

Dynamical cluster approximation with continuous lattice self-energyPeter Staar,¹ Thomas Maier,^{2,3} and Thomas C. Schulthess^{1,2,4}¹*Institute for Theoretical Physics, ETH Zurich, 8093 Zurich, Switzerland*²*Computer Science and Mathematics Division, Oak Ridge National Laboratory, Oak Ridge, Tennessee 37831, USA*³*Center for Nanophase Materials Sciences, Oak Ridge National Laboratory, Oak Ridge, Tennessee 37831, USA*⁴*Swiss National Supercomputing Center, ETH Zurich, 6900 Lugano, Switzerland*

(Received 29 March 2013; published 3 September 2013)

The dynamical cluster approximation (DCA) is a systematic extension beyond the single-site approximation in dynamical mean field theory, to include spatially nonlocal correlations in quantum many-body simulations of strongly correlated systems. We extend the DCA with a continuous lattice self-energy in order to achieve better convergence with cluster size. This method, which we call DCA⁺, cures the cluster-shape dependence problems of the DCA, without suffering from causality violations of previous attempts to interpolate the cluster self-energy. A practical approach based on standard inference techniques is given to deduce the continuous lattice self-energy from an interpolated cluster self-energy. We study the pseudogap region of a hole-doped two-dimensional Hubbard model and find that, in the DCA⁺ algorithm, the self-energy and pseudogap temperature T^* converge monotonously with cluster size. Introduction of a continuous lattice self-energy eliminates artificial long-range correlations and thus significantly reduces the sign problem of the quantum Monte Carlo cluster solver in the DCA⁺ algorithm compared to the normal DCA. Simulations with much larger cluster sizes thus become feasible, which, along with the improved convergence in cluster size, raises hope that precise extrapolations to the exact infinite cluster size limit can be reached for other physical quantities as well.

DOI: [10.1103/PhysRevB.88.115101](https://doi.org/10.1103/PhysRevB.88.115101)

PACS number(s): 71.10.Fd, 74.72.Kf, 71.27.+a

I. INTRODUCTION

The study of interacting electrons in a crystalline solid remains one of the most challenging problems of condensed matter physics. On a purely theoretical level, these models give us insight on spontaneous symmetry breaking, which leads to new ground states with exciting properties such as superconductivity. On a more practical level, the lattice models allow us to better understand materials in which the correlations between electrons determine their physical properties. The most famous examples of such materials are the high- T_c cuprates¹ and the recently discovered pnictides.² A better understanding of how the Cooper pairs are formed in these materials might lead us in the future to the creation of new materials with higher superconducting transition temperature.

One of the methods of choice to investigate interacting electrons on a lattice model is the dynamical mean field theory (DMFT),³ which in conjunction with model parameters derived from first-principles electronic-structure calculations^{4–8} is now capable of predicting spectral properties of transition-metal oxides⁹ and heavy-fermion materials.^{10–15} The study of the pairing mechanism in superconductors, however, requires inclusions of dynamic correlations between lattice sites, and hence the extension of DMFT beyond the single-site approximation. To this end, several quantum cluster extensions to DMFT have been developed during the past 15 years.^{16–19} Among these is the dynamical cluster approximation (DCA),^{19–21} a systematic extension to DMFT that includes nonlocal correlations through coarse graining in momentum space. The DCA relies on the assumption that the self-energy function is a localized function in real space. In infinite dimensions, it has been proven that the self-energy Σ is a delta function in real space,²² in which case this assumption trivially holds. In practice, we see that the locality increases with increasing dimension. This explains

why a single-site DMFT approach generally works better for three-dimensional (3D) materials, but fails to describe materials of quasi-one-dimensional (1D) or -two-dimensional (2D) nature.

The dynamical cluster approximation was developed to study materials of 2D nature by allowing the self-energy to be nonlocal. In the DCA, the infinite lattice problem is reduced to a finite-size quantum cluster impurity with periodic boundary conditions, embedded into a self-consistent mean field. This reduction is achieved via a coarse-graining procedure of the Green's function, in which the Brillouin zone is divided into N_c patches and the self-energy Σ is assumed to be constant on these patches. In this way, all correlations within the cluster are dealt with exactly, while long-range correlations outside the cluster are described via a mean field. If the cluster impurity problem is solved exactly, such as with quantum Monte Carlo (QMC) integration, the DCA will reproduce the exact solution of the lattice model in the limit of infinite cluster size.

In practice, the fermionic sign problem^{23,24} imposes an upper bound to the cluster size and a lower bound to the temperature which can be accessed. While small clusters have proven to give us an excellent qualitative insight on the physical phenomena,¹⁹ most physical quantities, such as the superconducting transition temperature T_c , converge poorly on the available small clusters.²⁵ The DCA can therefore not be used as a reliable method for quantitative predictions of those observables.

There are two important factors that influence the results of the DCA, both related to the choice of the cluster. The most obvious factor is the mean field approximation, which reduces the momentum anisotropy of the self-energy as the clusters become smaller. One can only avoid this error by considering clusters with a sufficiently large size. In practice, the critical cluster size is obtained by comparing physical

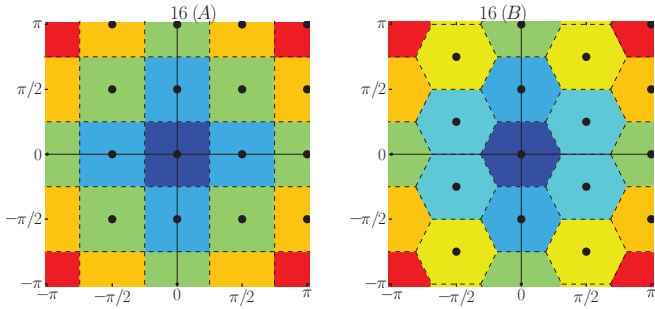


FIG. 1. (Color online) The positions of the cluster momenta $\{\vec{K}\}$ and shape of the patches for two 16-site DCA clusters. Notice that the 16B-site cluster does not have the same point-group symmetry as the Brillouin zone, leading to a lattice self-energy with a lower symmetry.

quantities on different cluster sizes. More complicated is the influence of the geometry of the cluster. There are a set of different clusters, all of which have the same cluster size but different shape and therefore different positions of the cluster momentum points. In Fig. 1, we show two 16-site clusters for which this is the case. The different positioning of the cluster momentum points in these two clusters leads to a different geometric shape of the coarse-graining patches and thus a different parametrization of the self-energy. This is illustrated in Fig. 2, where the momentum dependence of the DCA self-energy at the lowest Matsubara frequency is shown for the 16A- and 16B-site clusters introduced in Fig. 1. The relative error between the self-energies on the different clusters is close to 100% around the Fermi surface, making it unsuitable to derive any quantitative results from this calculation.

One can argue that the influence of the mean field approximation for clusters with the same size is similar. Therefore, the difference in results can be brought back to the shape of the coarse-graining patches. One example is the difference in superconducting transition temperature T_c between the 16A- and 16B-site clusters.²⁵ The role of the geometry has

been studied intensively by investigating the evolution of the magnetic and superconducting transition temperatures over different cluster sizes^{25,26} or by comparing the site occupancies of different clusters over a wide range of doping.^{27,28}

The geometric shape dependence of the self-energy is built into the DCA by construction since the DCA self-energy is expanded on the coarse-grain patches as²⁹

$$\Sigma(\vec{k}, \varpi_m) = \sum_i \phi_{\vec{K}_i}(\vec{k}) \Sigma_{\vec{K}_i}(\varpi_m). \quad (1)$$

Here, the set of patches $\{\phi_{\vec{K}_i}(\vec{k})\}$ is formally defined through the cluster momenta $\{\vec{K}_i\}$,

$$\phi_{\vec{K}_i}(\vec{k}) = \begin{cases} 1 & \forall j : |\vec{k} - \vec{K}_i| \leq |\vec{k} - \vec{K}_j|, \\ 0 & \exists j : |\vec{k} - \vec{K}_i| > |\vec{k} - \vec{K}_j| \end{cases} \quad (2)$$

and $\Sigma_{\vec{K}_i}(\varpi_m)$ is the cluster self-energy for momentum \vec{K}_i .

In this paper, we present an extension to the DCA that allows the self-energy to be expanded in an arbitrary large set of smooth basis functions, and thereby itself becoming a smooth function of momentum. The inclusion of a smooth self-energy into the framework of the DCA requires a different fundamental look at the algorithm. The resulting extended algorithm will be called DCA⁺, indicating an incremental generalization to the well-known DCA algorithm. The distinguishing feature of the DCA⁺ algorithm that sets it apart from the DCA algorithm is that cluster and lattice self-energies are in general different. In the DCA, the lattice self-energy $\Sigma(\vec{k})$ is a simple extension of the cluster self-energy $\Sigma_{\vec{K}_i}$ via the step function form in Eq. (1). It therefore has jump discontinuities between the patches. In the DCA⁺, the lattice self-energy is a function with continuous momentum dependence, which when coarse grained is equal to the cluster self-energy.

The focus of this paper is threefold. First, we will present the theoretical background of the DCA⁺ algorithm, without going into any practical details. Next, we introduce a practical implementation for the DCA⁺ algorithm and discuss in detail the numerical aspects of the lattice-mapping implementation.

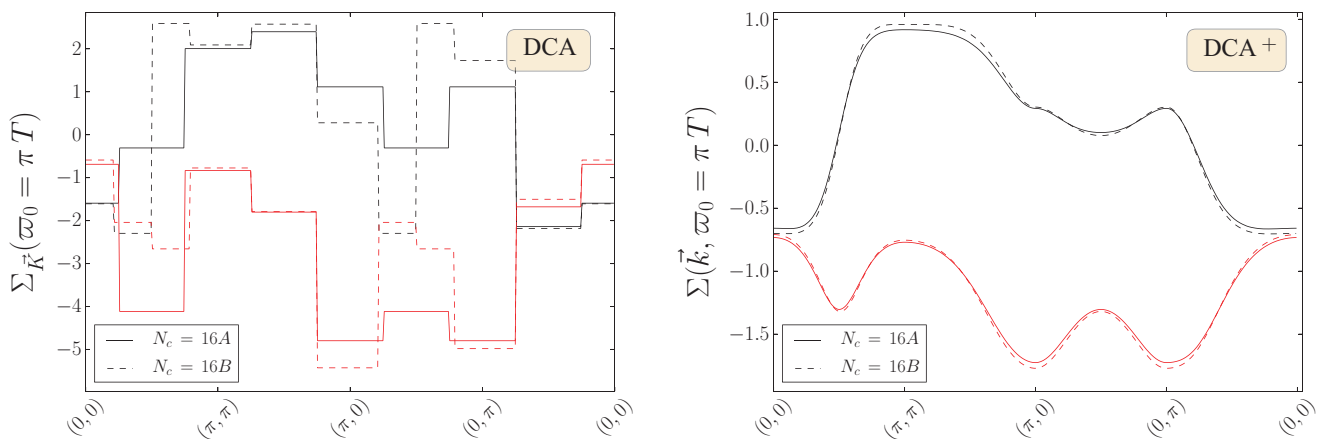


FIG. 2. (Color online) Momentum dependence of the DCA and DCA⁺ self-energies (red and black represent the imaginary and real parts, respectively) calculated on the 16A and 16B clusters in a half-filled Hubbard model with nearest-neighbor hopping $t = 1$, Coulomb interaction $U/t = 7$, and next-nearest-neighbor hopping $t'/t = -0.15$ at a temperature $T = 0.2$. For the DCA, one clearly sees a large difference between the self-energies of the two clusters at the section $(\pi, 0) \rightarrow (0, \pi)$, which is close to the Fermi surface and thus physically the most relevant part of the self-energy. In the DCA⁺, the self-energies of the two clusters agree very well.

Finally, we apply the DCA⁺ algorithm to the single-band Hubbard model in order to investigate the pseudogap behavior, which has recently been investigated in a systematic way with the DCA.^{27,28} In the theory section, we first derive the coarse-graining equations for the DCA⁺, which define how the lattice system is mapped onto an effective cluster problem. This will introduce the key concepts of the DCA⁺ approach on a general level. Next, we discuss the structure of the DCA⁺ algorithm in more detail. Here, we will pay special attention to the lattice mapping, i.e., the inversion of the coarse graining, where a lattice self-energy is estimated from a given cluster self-energy. We will show that the lattice mapping is only possible if the DCA assumption of a localized self-energy in real space is upheld. In the implementation part, we will discuss the lattice mapping in detail on a practical level. In this paper, we propose to perform the lattice mapping in two steps. First, we interpolate the self-energy obtained from the cluster solver. Next, we deconvolute the interpolated cluster self-energy, where the patch $\phi_{\vec{0}}(\vec{k})$ is used as the convolution kernel. In the physics section, we will use the DCA⁺ to investigate the pseudogap behavior in the low-doping region of the two-dimensional Hubbard model. The self-energy in this phase is known to be strongly momentum dependent and we will show that the pseudogap transition temperature T^* converges faster with regard to the cluster size in the DCA⁺ than in the DCA.

All calculations in this paper were performed for a single-band Hubbard model

$$H = \sum_{ij} t_{ij} c_{i\sigma}^\dagger c_{j\sigma} + U \sum_i n_{i\uparrow} n_{i\downarrow}. \quad (3)$$

Here, $c_{i\sigma}^\dagger$ ($c_{i\sigma}$) creates (destroys) an electron with spin σ on lattice site i and $n_{i\sigma} = c_{i\sigma}^\dagger c_{i\sigma}$ is the corresponding number operator. The hopping matrix t_{ij} includes nearest- ($t = 1$) and next-nearest- (t') neighbor hopping and U is the onsite Coulomb repulsion. The effective cluster problem of the DCA and DCA⁺ is solved with a continuous-time auxiliary-field quantum Monte Carlo algorithm.^{30,31}

II. THEORY

In this section, we present the generic structure of the DCA⁺ algorithm, without going into any implementation details. First, we introduce the key features of the DCA⁺ algorithm that distinguish it from the DCA, and show that the latter is just a specialization of the former. Next, we present a geometric interpretation of the DCA⁺ algorithm in terms of the functional representation space of the self-energy. This interpretation provides guidance for how cluster-dependent features are incorporated into the lattice self-energy, and offers insights for the derivation of a practical implementation of the DCA⁺ algorithm that will be discussed in the following section. In order to keep the notation simple, we will omit the frequency parameter ω in all equations. Furthermore, all single-particle functions defined on the impurity cluster are represented by a subscript on the cluster momenta (e.g., the cluster self-energy $\Sigma_{\vec{k}}$), while the continuous lattice single-particle functions will have the usual dependence on the momentum vector \vec{k} [e.g., the lattice self-energy $\Sigma(\vec{k})$].

An overline over the quantity signifies that the latter has been coarse grained.

A. DCA and DCA⁺ formalisms

A system of interacting electrons on a lattice is generally described by a Hamiltonian $H = H_0 + H_{\text{int}}$, where the kinetic energy H_0 is quadratic in the fermion operators and the interaction H_{int} is quartic. Its free energy Ω may be written in terms of the exact single-particle Green's function G as

$$\Omega[G] = \text{Tr} \ln(-G) + \Phi[G] - \text{Tr}[(G_0^{-1} - G^{-1})G]. \quad (4)$$

Here, we have used a matrix notation for the Green's function G of the interacting system described by H and the Green's function G_0 of the noninteracting system described by H_0 . $\Phi[G]$ is the Luttinger-Ward functional³² given by the sum of all vacuum-to-vacuum "skeleton" diagrams drawn with G . The self-energy Σ is obtained from the functional derivative of $\Phi[G]$ with respect to G (Refs. 33 and 34):

$$\Sigma = \frac{\delta \Phi[G]}{\delta G}, \quad (5)$$

and is related to the Green's function via the Dyson equation

$$G_0^{-1} - G^{-1} = \Sigma. \quad (6)$$

These two relations imply that the free energy is stationary with respect to G , i.e., $\delta \Omega[G]/\delta G = 0$. In principle, the exact Green's function G and self-energy Σ can be determined from the self-consistent solution of Eqs. (5) and (6). However, since the functional $\Phi[G]$ is usually unknown, an approximation is required that replaces the exact $\Phi[G]$ by a known or a computable functional. Conserving approximations replace the exact $\Phi[G]$ by an approximate functional, which sums up certain subclasses of diagrams that are thought to capture the dominant physics. In general, this results in a weak coupling approximation. A different approach is taken in the DCA: rather than approximating the Luttinger Ward Φ , the functional representation space of the Green's function is reduced by replacing the exact Green's function $G(\vec{k})$ by a *coarse-grained* Green's function $\bar{G}_{\vec{k}}$ in momentum space defined as

$$\bar{G}_{\vec{k}} = \int d\vec{k} \phi_{\vec{k}}(\vec{k}) G(\vec{k}), \quad (7)$$

where the coarse-graining functions $\phi_{\vec{k}}(\vec{k})$ have been defined in Eq. (2). We note that approximating G in this way corresponds to an approximation of the Laue function $\Delta_{\vec{k}_1+\vec{k}_3, \vec{k}_2+\vec{k}_4}$, which expresses momentum conservation at each vertex in the diagrams defining Φ .^{20,21} For the single-site DMFT approximation ($N_c = 1$), $\phi(\vec{k})$ is constant over the entire Brillouin zone, and consequently the Laue function is replaced by $\Delta_{\text{DMFT}} = 1$, i.e., momentum conservation is disregarded. For a finite-size DCA cluster ($N_c > 1$), the Laue function restores momentum conservation for the cluster momenta \vec{K} and reads as, in terms of the $\phi_{\vec{k}}(\vec{k})$,

$$\Delta_{\text{DCA}}(\vec{k}_1, \vec{k}_2, \vec{k}_3, \vec{k}_4) = \delta_{\vec{k}_1+\vec{k}_3, \vec{k}_2+\vec{k}_4} \phi_{\vec{k}_1}(\vec{k}_1) \times \phi_{\vec{k}_2}(\vec{k}_2) \phi_{\vec{k}_3}(\vec{k}_3) \phi_{\vec{k}_4}(\vec{k}_4). \quad (8)$$

By replacing the exact Laue function with its DCA approximation in the Luttinger-Ward functional, the momentum

integrals over the Green's functions in the diagrams defining the Φ functional are reduced to sums over the finite set of coarse-grained Green's functions defined in Eq. (7). This way, $\Phi[\bar{G}]$ becomes identical to the Luttinger-Ward functional of a finite-size cluster and the computation of the corresponding self-energy

$$\Sigma_{\vec{k}}^{\text{DCA}} = \delta\Phi[\bar{G}_{\vec{k}}]/\delta\bar{G}_{\vec{k}} \quad (9)$$

becomes feasible. As such, within the DCA approximation, the free-energy functional $\Omega[G]$ becomes

$$\Omega_{\text{DCA}}[G] = \text{Tr} \ln(-G) + \Phi[\bar{G}] - \text{Tr}[(G_0^{-1} - G^{-1})G].$$

From stationarity of the free energy $\delta\Omega[G]/\delta G = 0$, one obtains the Dyson equation within the DCA

$$G_0^{-1}(\vec{k}) - G^{-1}(\vec{k}) = \sum_{\vec{k}} \phi_{\vec{k}}(\vec{k}) \Sigma_{\vec{k}}^{\text{DCA}}. \quad (10)$$

Here, the right-hand side follows from $\delta\bar{G}_{\vec{k}}/\delta G = \phi_{\vec{k}}(\vec{k})$ and $\delta\Phi[\bar{G}_{\vec{k}}]/\delta\bar{G}_{\vec{k}} = \Sigma_{\vec{k}}^{\text{DCA}}$. Equations (7), (9), and (10) form a closed set of equations which is solved iteratively until self-consistency is reached. This is the DCA algorithm. Following Eq. (10), the self-energy $\Sigma(\vec{k})$ of the lattice Green's function $G(\vec{k})$, which is used to compute the coarse-grained Green's function in Eq. (7), is approximated by a piecewise constant continuation of the cluster self-energy $\Sigma_{\vec{k}}^{\text{DCA}}$, which changes between different momentum patches but is constant within a given patch

$$\Sigma(\vec{k}) = \sum_{\vec{k}} \Sigma_{\vec{k}}^{\text{DCA}} \phi_{\vec{k}}(\vec{k}). \quad (11)$$

With the DCA⁺ algorithm we introduce in this paper, the DCA framework is extended to allow for a more general relationship between the lattice self-energy $\Sigma(\vec{k})$ and cluster self-energy $\Sigma_{\vec{k}}$ than that in Eq. (11). In the DCA⁺, in analogy with Eq. (7), we only demand the cluster self-energy to be equal to the coarse-grained lattice self-energy

$$\bar{\Sigma}_{\vec{k}} = \int d\vec{k} \phi_{\vec{k}}(\vec{k}) \Sigma(\vec{k}). \quad (12)$$

In the DCA algorithm, this requirement is trivially satisfied since according to Eq. (11), $\Sigma(\vec{k})$ is set to the cluster self-energy $\Sigma(\vec{K})$ for momenta \vec{k} in patch P_i . However, it is important to realize that Eq. (12) allows for a more general approximation of the lattice $\Sigma(\vec{k})$, which, for example, can retain its smooth momentum dependence instead of the DCA step-function character. To proceed, it is convenient for our purposes to express the free energy as a functional of the self-energy. By following the work of Potthoff,^{35,36} we eliminate the Green's function G in favor of the self-energy Σ to write the free energy as a functional of the self-energy Σ :

$$\Omega[\Sigma] = -\text{Tr} \ln[-(G_0^{-1} - \Sigma)] + (\mathcal{L}\Phi)[\Sigma]. \quad (13)$$

Here, the functional $(\mathcal{L}\Phi)[\Sigma]$ is obtained from $\Phi[G]$ through a Legendre transformation

$$(\mathcal{L}\Phi)[\Sigma] = \Phi - \text{Tr}[\Sigma G]. \quad (14)$$

Replacing $\Sigma(\vec{k})$ in $(\mathcal{L}\Phi)[\Sigma]$ with the coarse-grained self-energy in Eq. (12), i.e., $\Sigma(\vec{k}) \approx \sum_{\vec{k}} \phi_{\vec{k}}(\vec{k}) \bar{\Sigma}_{\vec{k}}$, then yields

$$(\mathcal{L}\Phi)[\Sigma] = \Phi - \sum_{\vec{k}} \bar{\Sigma}_{\vec{k}} \bar{G}_{\vec{k}}, \quad (15)$$

where $\bar{G}_{\vec{k}}$ is the coarse-grained Green's function defined in Eq. (7). If this functional is used in the free energy in Eq. (13), one obtains at stationarity, $\delta\Omega[\Sigma]/\delta\Sigma = 0$,

$$[G_0^{-1}(\vec{k}) - \Sigma(\vec{k})]^{-1} = \sum_{\vec{k}} \phi_{\vec{k}}(\vec{k}) \bar{G}_{\vec{k}}. \quad (16)$$

Here, the right-hand side follows from $\delta\bar{\Sigma}_{\vec{k}}/\delta\Sigma = \phi_{\vec{k}}(\vec{k})$ and $(\mathcal{L}\Phi)[\bar{\Sigma}_{\vec{k}}]/\delta\bar{\Sigma}_{\vec{k}} = -\bar{G}_{\vec{k}}$. Using the identity $\int d\vec{k} \phi_{\vec{k}}(\vec{k}) \phi_{\vec{k}'}(\vec{k}) = \delta_{\vec{k}, \vec{k}'}$ and multiplying both sides with $\int d\vec{k} \phi_{\vec{k}}(\vec{k})$ results in the DCA⁺ coarse-graining equation

$$\bar{G}_{\vec{k}} = \int d\vec{k} \phi_{\vec{k}}(\vec{k}) [G_0^{-1}(\vec{k}) - \Sigma(\vec{k})]^{-1}. \quad (17)$$

We note that in contrast to the DCA algorithm, the lattice self-energy $\Sigma(\vec{k})$ enters in the coarse-graining step. It is related to the cluster self-energy $\Sigma_{\vec{k}}$ through Eq. (12), i.e., its coarse-grained result must be equal to $\Sigma(\vec{K})$. The special choice $\Sigma(\vec{k}) = \sum_{\vec{k}} \phi_{\vec{k}}(\vec{k}) \Sigma_{\vec{k}}$ satisfies this requirement and recovers the DCA algorithm. But in general, $\Sigma(\vec{k})$ needs to only satisfy Eq. (12), i.e., one has more freedom in determining a lattice self-energy $\Sigma(\vec{k})$ from the cluster $\Sigma(\vec{K})$. In the DCA⁺ algorithm, we take advantage of this freedom to derive a $\Sigma(\vec{k})$ that retains a smooth \vec{k} dependence and thus is more physical than the piecewise constant $\Sigma(\vec{k})$ of the DCA. As in the DCA, the cluster self-energy $\Sigma_{\vec{k}}$ may be determined from the solution of an effective cluster problem described by $(\mathcal{L}\Phi)[\Sigma]$ as a functional of the coarse-grained propagator $\Sigma[\vec{K}] = \Sigma[\bar{G}(\vec{K})]$. This, together with Eqs. (12) and (17), forms the basis of the DCA⁺ algorithm.

A detailed description of the algorithm will be given in the implementation section. Evidently, determining the lattice self-energy $\Sigma(\vec{k})$ from the cluster self-energy $\Sigma_{\vec{k}}$ through inversion or deconvolution of Eq. (12) presents a difficult task.

B. Structure of a DCA⁺ cluster calculation

Since the lattice self-energy $\Sigma(\vec{k})$ no longer is restricted to Eq. (1), it can be expanded into an arbitrary set of smooth basis functions $\{\mathcal{B}_i(\vec{k})\}$, such as cubic splines or crystal harmonics, i.e.,

$$\Sigma(\vec{k}) = \sum_i \mathcal{B}_i(\vec{k}) \sigma_i. \quad (18)$$

Here, σ_i are the expansion coefficients of the lattice self-energy corresponding to the basis function $\mathcal{B}_i(\vec{k})$. Contrary to the DCA, the coarse-graining patches $\phi_{\vec{k}}(\vec{k})$ in the DCA⁺ are not linked in any shape or form to the basis functions in which we expand the lattice self-energy. As was mentioned in the previous section, the DCA⁺ maps the full lattice problem into a cluster impurity problem embedded into a mean field by coarse graining both the lattice self-energy and lattice Green's function. The cluster mapping in the DCA⁺ is thus very similar to the cluster mapping in the DCA, with the exception that we

use a continuous lattice self-energy in the coarse graining of the Green's function

$$\begin{aligned}\bar{\Sigma}_{\bar{K}} &= \frac{N_c}{V_{\text{BZ}}} \int_{\text{BZ}} d\bar{k} \phi_{\bar{K}}(\bar{k}) \Sigma(\bar{k}), \\ \bar{G}_{\bar{K}} &= \frac{N_c}{V_{\text{BZ}}} \int_{\text{BZ}} d\bar{k} \phi_{\bar{K}}(\bar{k}) [[G^0(\bar{k})]^{-1} - \Sigma(\bar{k})]^{-1}.\end{aligned}\quad (19)$$

Equation (19) can now be simplified by using the explicit expansion of the lattice self-energy in Eq. (18):

$$\bar{\Sigma}_{\bar{K}_i} = \sum_j \left(\underbrace{\int d\bar{k} \phi_{\bar{K}_i}(\bar{k}) \mathcal{B}_j(\bar{k})}_{= P_{i,j}} \right) \sigma_j. \quad (20)$$

Here, $P_{i,j}$ is a projection operator, defined by coarse graining the basis function \mathcal{B}_j over patch i . Note that in the DCA, this projection operator becomes the identity operation $\delta_{i,j}$. Hence, the coarse graining of the lattice self-energy in the DCA is an implicit operation ($\sigma_i \equiv \bar{\Sigma}_{\bar{K}_i}$), while in the DCA⁺ it becomes explicit.

With the introduction of the cluster mapping in the DCA⁺ in Eq. (20), the lattice mapping is conceptually well defined as long as the inverse of the projection operator P exists. Assuming that P^{-1} exists, we can retrieve the expansion coefficients of the lattice self-energy from the self-energy of the cluster solver $\Sigma_{\bar{K}}$ in a straightforward manner:

$$\sigma_j = \sum_i (P^{-1})_{i,j} \Sigma_{\bar{K}_i}. \quad (21)$$

This closes the DCA⁺ iteration and allows us to carry out a self-consistent calculation.

In Fig. 3, we have summarized the generic structure of the DCA⁺ algorithm, without specifying yet any implementation details of the lattice mapping. In the ‘‘cluster-mapping’’ step, the lattice Green's function and self-energy are coarse grained onto the patches defined by $\Phi_{\bar{K}}(\bar{k})$ to give $\bar{G}_{\bar{K}}$ and $\bar{\Sigma}_{\bar{K}}$, respectively. A cluster-solver algorithm such as QMC is then used to calculate, from the corresponding bare Green's function $G_{0,\bar{K}}$, the interacting Green's function and self-energy $\Sigma_{\bar{K}}$ on the cluster. In the ‘‘lattice-mapping step,’’ which is missing in the standard DCA algorithm, an estimate for the lattice self-energy $\Sigma(\bar{k})$ is then computed through inversion of the projection operator $P_{i,j}$. The lattice self-energy then enters the next cluster-mapping step via the lattice Green's function $G(\bar{k})$. In the implementation section of this paper, we will describe in detail how the lattice mapping can be done in a numerically stable way.

Due to the distinction between the lattice and cluster self-energy in the DCA⁺ algorithm, we can not use the convergence criteria of the DCA. In the latter, convergence is reached if the self-energy (lattice or cluster) of the previous iteration is equal to the current one. If one monitors only convergence on the lattice self-energy in the DCA⁺ algorithm, one might stop the iterations although the cluster solver still produces a cluster self-energy $\Sigma_{\bar{K}}$ that differs from the coarse-grained lattice self-energy $\bar{\Sigma}(\bar{K})$. This would indicate that the DCA⁺ does not converge to a stationary point of the free-energy functional Ω . To avoid such a problem, we demand that convergence is reached only when the coarse-grained lattice self-energy $\bar{\Sigma}(\bar{K})$

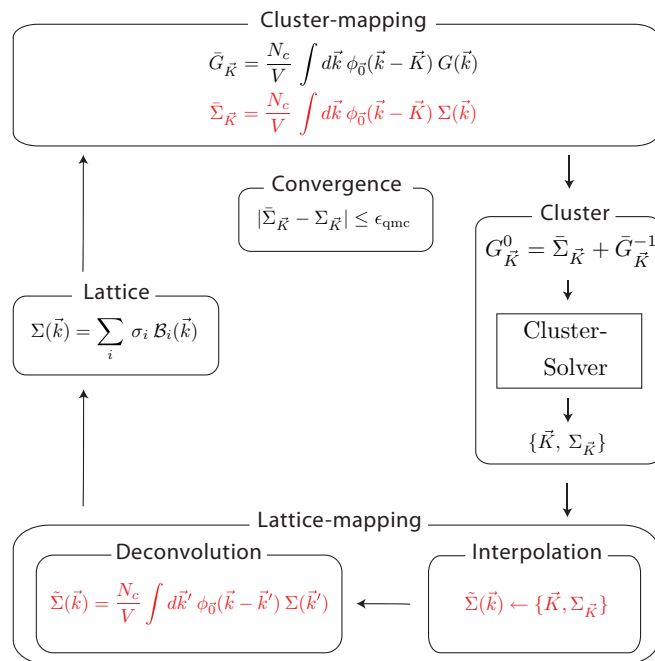


FIG. 3. (Color online) The generic structure of a self-consistent DCA⁺ algorithm, in which the cluster and lattice mapping play a central role in order to connect the continuous lattice self-energy $\Sigma(\bar{k})$ with the cluster self-energy $\Sigma_{\bar{K}}$. Convergence is reached when the cluster solver produces a cluster self-energy $\Sigma_{\bar{K}}$ equal to the coarse-grained self-energy $\bar{\Sigma}_{\bar{K}} \equiv \bar{\Sigma}(\bar{K})$.

and the cluster self-energy $\Sigma_{\bar{K}}$ agree to within the Monte Carlo sampling error.

It is important to note that the proposed algorithm is fundamentally different from a simple interpolation of the cluster self-energy $\Sigma_{\bar{K}}$ between the cluster momenta \bar{K} . A smooth interpolation will almost certainly fail to satisfy Eq. (12), i.e., the main requirement of the DCA⁺ that the coarse-grained lattice $\Sigma(\bar{k})$ is equal to the cluster $\Sigma_{\bar{K}}$. Such a procedure was proven in Ref. 20 to lead to causality violations when the cluster self-energy is added back to the inverse coarse-grained propagator in the ‘‘cluster-exclusion’’ step to avoid overcounting of self-energy diagrams. In the DCA⁺, the lattice self-energy is different from an interpolated cluster self-energy and the self-energy that enters the cluster-exclusion step is given by the coarse-grained lattice self-energy. Because of this, the proof given in Ref. 20 does not apply and the DCA⁺ algorithm is not automatically plagued by causality problems. Although we do not have a rigorous proof that the DCA⁺ algorithm remains causal, we have never encountered any causality violations in the application of this method to the single-band Hubbard model.

The projection operator $P_{i,j}$ plays a central role in the implementation of the DCA⁺ algorithm. In order to obtain a self-consistent algorithm, it is conceptually clear that the projection operator has to be invertible. In practice, however, this might not be straightforward to achieve. An intuitive understanding of this operator is developed in Appendix A, where we discuss how the projection operator influences the choice of the cluster, and we show that its inverse only exists

if the DCA locality assumption for the lattice self-energy is satisfied.

C. Role of the cluster in the DCA⁺

In the DCA algorithm, the real-space cluster takes a central role. It completely defines the basis functions in which the self-energy is expanded. Furthermore, the real-space cluster dictates how the lattice is mapped on the cluster through the coarse-graining procedure. Consequently, solutions obtained with the DCA algorithm usually dependent on the particular choice (shape) of the cluster. In practice, this leads to a very good qualitative description of the physics, but prohibits quantitative analysis, as calculated physical quantities strongly depend on cluster shape. In the DCA⁺, we start from an expansion of the self-energy into an arbitrary set of basis functions. In this way, the influence of the real-space cluster is reduced since it does not dictate the basis functions on which the self-energy is expanded. The real-space cluster only specifies how the cluster is mapped on the lattice through the shape of the coarse-graining patches. Consequently, the focus in the DCA⁺ shifts from the real-space cluster to the projection operator $P_{i,j}$. This operator embodies the quantum cluster approximation of the DCA⁺ since it connects the cluster self-energy with the lattice self-energy in a purely geometric way. The projection operator is only defined by the set of basis functions of the lattice self-energy and the real-space cluster and not subjected in any way to physical parameters (such as temperature, band structure, interaction terms, ...). This purely geometric property of the projection operator allows us to find *a priori* the necessary conditions to which the cluster self-energy has to be subjected, in order to allow for a self-consistent, cluster-independent DCA⁺ calculation. These necessary conditions that follow from the discussion in the previous subsections and Appendix A are as follows:

(i) In order to perform a self-consistent DCA⁺ calculation, the cluster self-energy has to converge in \mathcal{I}_ϵ , which is the part of the images space of the projection operator that is spanned by its eigenvectors with eigenvalues larger than a small, positive parameter ϵ .

(ii) In order to perform a cluster-independent DCA⁺ calculation on the clusters A and B , the cluster self-energy needs to converge on the intersection of the image spaces of both projectors ($\mathcal{I}_\epsilon^A \cap \mathcal{I}_\epsilon^B$).

III. IMPLEMENTATION

In the last section and in Appendix A, we have introduced a projection operator $P_{i,j}$ and shown its involvement in the cluster and lattice mapping. Via a geometric consideration, we have shown conceptually that its inverse exists as long as the expansion coefficients $\langle \bar{\Sigma}_{\vec{k}}, e_\lambda(\vec{k}) \rangle$ of the cluster self-energy vanish rapidly in the image space \mathcal{I}_ϵ of the projection operator $P_{i,j}$. At closer inspection, the lattice mapping is thus a two-stage process. First, we need to determine the expansion coefficients of the cluster self-energy. To this end, we will propose an interpolation technique, which is motivated from the analytical properties of the self-energy. The interpolated cluster self-energy $\bar{\Sigma}_{\vec{k}_j}$ is then used to compute the inner product $\langle \bar{\Sigma}_{\vec{k}_j}, e_\lambda(\vec{k}_j) \rangle$ with the eigenfunctions of the projection operator $P_{i,j}$, which gives the expansion coefficients of the

cluster self-energy. Second, we need to deconvolute the interpolated cluster self-energy on the image space \mathcal{I}_ϵ , where we need to determine the optimal value for the parameter ϵ . If the latter is too large, the self-consistency can not be reached. If ϵ is too small, the lattice mapping will become numerically unstable due to the division of small eigenvalues. To solve this problem, we adapt the Richardson-Lucy deconvolution algorithm, which inverts Eq. (20) in a numerically stable way.

A. Interpolation

In the context of tight-binding models, one of the most successful algorithms to interpolate its band structure is the Wannier interpolation method.³⁷ It finds its justification in the localized nature of Wannier orbitals, from which the tight-binding models are derived. Since the self-energy is a correction to the band structure due the interaction between the electrons, the Wannier interpolation method seems a suitable interpolation algorithm. Okamoto *et al.*³⁸ have examined this possibility implicitly, by expanding the lattice self-energy $\Sigma(\vec{k})$ into the cubic-harmonic basis functions $\{C_{\vec{K}}(\vec{k})\}$:

$$\begin{aligned} \Sigma(\vec{k}) &= \sum_{\vec{K}} C_{\vec{K}}(\vec{k}) \Sigma_{\vec{K}}, \\ C_{\vec{K}}(\vec{k}) &= \frac{1}{N_c} \sum_{\vec{R}} e^{i\vec{R}\vec{k}} e^{-i\vec{R}\vec{K}}. \end{aligned} \quad (22)$$

This approach only works when the self-energy $\Sigma_{\vec{K}}$ is sufficiently smooth, such that the real-space self-energy $\Sigma_{\vec{R}}$ converges on the cluster in real space. Notice that the latter is implicitly computed in Eq. (22) since

$$\Sigma(\vec{k}) = \sum_{\vec{K}} C_{\vec{K}}(\vec{k}) \Sigma_{\vec{K}} = \sum_{\vec{R}} e^{-i\vec{R}\vec{k}} \underbrace{\frac{1}{N_c} \sum_{\vec{K}} e^{i\vec{R}\vec{K}} \Sigma_{\vec{K}}}_{=\Sigma_{\vec{R}}}.$$

The sum over all lattice points can now be split into two terms. In the first term, we run over all lattice points within the cluster radius. In the second term, we sum over all the remaining points in the lattice:

$$\begin{aligned} \Sigma(k) &= \sum_{\vec{R}} e^{-i\vec{R}\vec{k}} \Sigma_{\vec{R}} \\ &= \sum_{|\vec{R}| < R_c} e^{-i\vec{R}\vec{k}} \Sigma_{\vec{R}} + \sum_{|\vec{R}| \geq R_c} e^{-i\vec{R}\vec{k}} \Sigma_{\vec{R}}. \end{aligned} \quad (23)$$

If correlations have longer range, $\Sigma_{\vec{R}_i}$ will no longer converge on the cluster in real space. This is clearly illustrated in Fig. 4, where we show the self-energy $\Sigma_{\vec{R}}$ for a $N_c = 100$ -site cluster with $U/t = 7$ for various temperatures. At high temperatures ($T \geq 0.25$), the system is only weakly correlated. The self-energy $\Sigma_{\vec{R}}$ in this temperature range is contained within the cluster radius $R_c = 5$. For lower temperatures, it is clear that $\Sigma_{\vec{R}}$ extends beyond R_c . Applying the Wannier interpolation scheme according to Eq. (22) to such correlated systems is simply not allowed since the expansion coefficients $\Sigma_{\vec{R}}$ outside the cluster can not be assumed to be zero. A straightforward application of Eq. (22) will lead to ringing and eventually to causality violations. The latter was observed by Okamoto *et al.*,³⁸ and could only partially be resolved

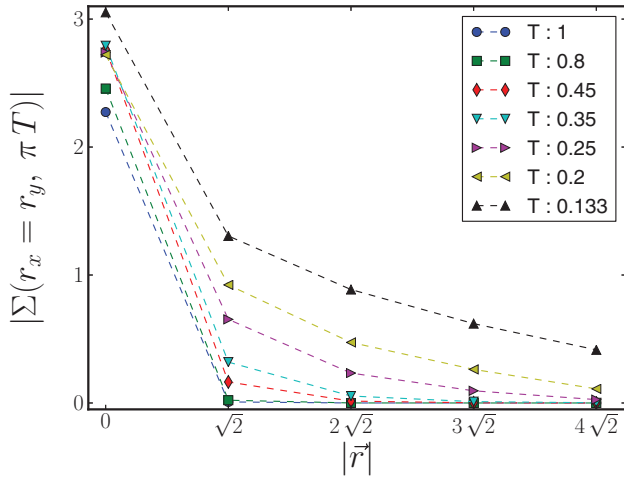


FIG. 4. (Color online) The decay of Σ_R for a $N_c = 100$ -site cluster with $U/t = 7$ and $t'/t = 0$ for various temperatures at half-filling. For high temperatures ($T \leq 0.3$), the system is only weakly correlated and Σ_R will rapidly decay. For low temperatures, the correlations exceed the cluster radius $R_c = 5$.

by introducing low-pass filtering schemes. The applicability of this approach is very limited, due to a lack of a general framework to determine these filters.

1. Formalism of the interpolation

From the previous section, it has become clear that the interpolation techniques such as Eq. (22) can only work if the function converges on the finite (and often small) basis set. The rate of convergence depends critically on the choice of the basis functions. Consider, for example, the free Green's function G^0 of the single-band Hubbard model in Eq. (3):

$$G^0(\vec{k}, \varpi) = [i\varpi + \epsilon(\vec{k})]^{-1}. \quad (24)$$

While this Green's function G^0 will converge poorly on the cubic harmonics of the lattice for small frequency ϖ , it is straightforward to see that $[G^0]^{-1}$ will be completely converged on a four-site cluster. This simple example shows how one can extend the interpolation idea introduced by Okamoto *et al.*³⁸ Given an injective transformation \mathcal{T} , we can write

$$\begin{aligned} \mathcal{F}(\vec{k}) &= \mathcal{T}^{-1}[\mathcal{T}[\mathcal{F}(\vec{k})]] \\ &= \mathcal{T}^{-1}\left[\sum_{\vec{k}} \mathcal{C}_{\vec{k}}(\vec{k}) \mathcal{T}[\mathcal{F}_{\vec{k}}]\right]. \end{aligned} \quad (25)$$

The method of operation to interpolate a function becomes now clear. Find an injective (and preferably analytical) transformation \mathcal{T} , such that the transformed function values converge on the chosen basis functions. Use this expansion to compute the transformed function values on arbitrary k points. Finally, apply the inverse transformation \mathcal{T}^{-1} on the transformed function values in order to obtain the desired interpolated function values on arbitrary k points.

This approach has many advantages. First, it provides a measure that indicates when the interpolation procedure works or fails. If $\mathcal{T}[\Sigma_{\vec{k}}]$ does not converge on the basis set, one is not allowed to perform an interpolation. Second, this interpolation

procedure does not introduce *extra information*; filtering schemes and other numerical tricks to ensure causality, on the other hand, introduce extra, undesirable structure into the interpolated functions. By using filtering schemes or other numerical tricks to assure causality, we introduce extra structure in the function that is to be interpolated, which is undesirable. Third, if the transformation \mathcal{T} is analytical, we will not break the analyticity of the interpolated function. For Green's functions and their derived functions such as the self-energy, analyticity is an important property. In arbitrary interpolation schemes such as splines³⁹ or radial-basis expansions,⁴⁰ this analyticity is often broken. The obtained interpolating function is therefore questionable from a physics point of view. The challenge of this approach is naturally the search for a correct transformation \mathcal{T} . Notice that \mathcal{T} can be different for different functions since the only requirements are injectivity and convergence on the chosen basis set. In the next sections, we will propose such a transformation for the self-energy Σ . The proposed transformation will be motivated by physical and analytical properties of the self-energy.

2. Interpolation on large clusters

Since the imaginary part of the self-energy is strictly negative in the upper half of the complex plane⁴¹

$$\text{Im}[\Sigma(\vec{k}, i\varpi > 0)] < 0, \quad (26)$$

we can introduce an injective transformation \mathcal{T} that preserves the analyticity of the self-energy {since $\text{Im}[\Sigma(\vec{k}, \varpi)] < 0$, we will not introduce any new poles in the upper-half plane by inverting the function}:

$$\mathcal{T}(\Sigma) = [\Sigma - \alpha i]^{-1}, \quad \text{with } \alpha > 0. \quad (27)$$

Note that this form is similar to the cumulant used in Ref. 42 for interpolation, where it was shown to be a better quantity to interpolate than the self-energy directly. Due to the property shown in (26), the transformation \mathcal{T} will map the self-energy Σ into a bounded function, irrespective of how spiky the self-energy Σ is. Notice also that we first shift the imaginary part of the self-energy down by αi , in order to avoid introducing poles due to the Monte Carlo statistical noise. Consequently, the function $\mathcal{T}(\Sigma)$ will now be localized in real space, and we can safely perform an expansion of the function $\mathcal{T}(\Sigma)$ over cubic harmonics. We have illustrated this process in Fig. 5 by applying our interpolation procedure to a 100-site cluster at a temperature $T = 0.2$ at half-filling. In Fig. 5(a), we show, respectively, the computed values of the cluster self-energy $\Sigma_{\vec{k}}$ and its interpolation $\Sigma_{\vec{k}}$ along a high-symmetry line in the Brillouin zone. Notice that the imaginary part of the interpolation function remains at all times negative! In Fig. 5(b), the transformed function $\mathcal{T}[\Sigma_{\vec{k}}]$ is shown, together with its interpolating function. Clearly, the transformation \mathcal{T} has reduced the sharp features in the self-energy, and the function has become smoother. In Figs. 5(c) and 5(d), we show the Fourier transform from, respectively, the interpolated self-energy $\Sigma(\vec{k})$ and the transformed values $\mathcal{T}[\Sigma_{\vec{k}}]$. The large difference in the convergence radii is clear and shows the effectiveness of our indirect approach compared to a direct one. This result is not a coincidence. In Appendix B, we have proven in a rigorous way the pointwise convergence.

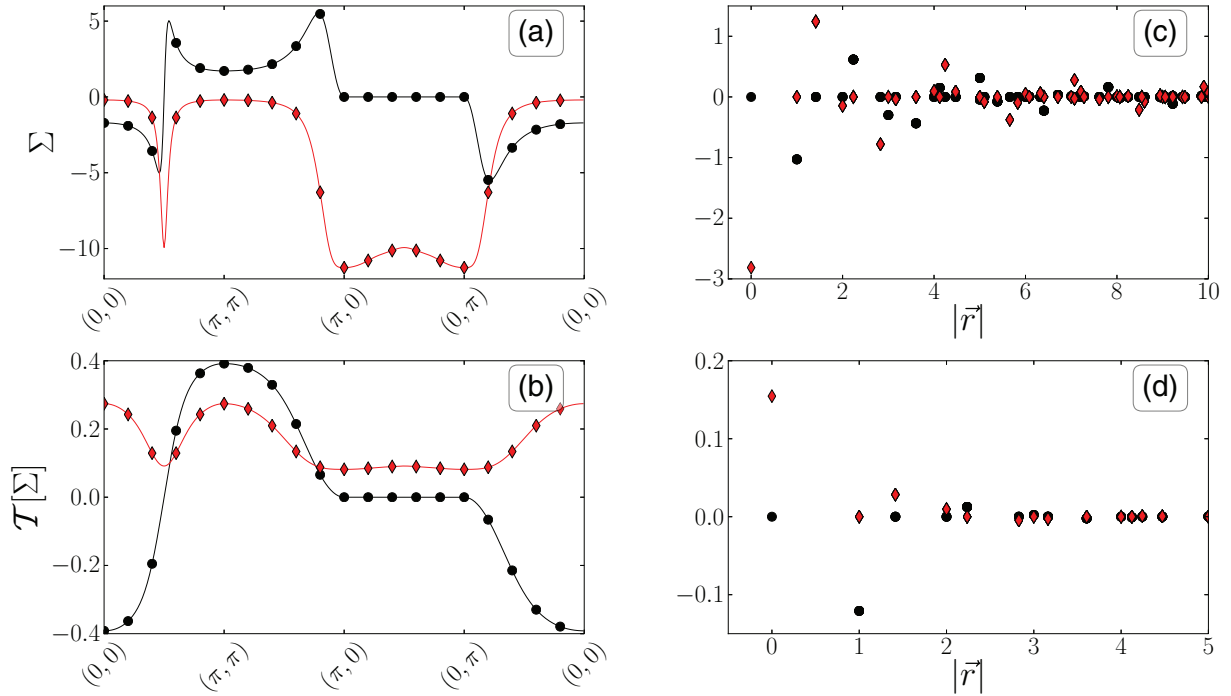


FIG. 5. (Color online) Interpolation procedure for the self-energy $\Sigma_{\vec{k}}$ at the lowest Matsubara frequency for a 100-site cluster at a temperature $T = 0.2$, $U/t = 7$, and $t' = 0$ at half-filling. (a) The interpolated function $\Sigma(\vec{k})$ is a smooth function through the results $\Sigma_{\vec{k}}$ obtained from the QMC cluster solution, where the circles and diamonds represent, respectively, the real and imaginary parts. (b) The transformed function $\mathcal{T}[\Sigma]$ smooths the self-energy function, making it suitable for a cubic-harmonics expansion. (c) The Fourier transform of the interpolated function $\Sigma(k)$. Notice that the tails expand much further than the cluster radius $R_c = 5$. (d) The Fourier transform of the function $\mathcal{T}[\Sigma_{\vec{k}}]$. The convergence is reached at $R_c = 3$.

3. Interpolation on small clusters

For certain parameter sets, the fermionic sign problem prevents the investigation of large enough clusters, for which $\mathcal{T}[\Sigma]$ will converge. In this case, we recommend to interpolate the $\mathcal{T}[\Sigma]$ using cubic splines instead of interpolating the latter with the earlier proposed Wannier interpolation. Since $\mathcal{T}[\Sigma]$ is a much smoother function, cubic splines can still perform reasonably well, even in the case of small clusters. The self-energy on the other hand will not be smooth, and a straightforward spline interpolation will lead to overshoots or ringing, which in turn might lead to an acausal self-energy. This particular phenomenon has been studied extensively by Okamoto *et al.*³⁸ The ringing might be cured by the use of tension splines,⁴³ in which case a tension parameter is introduced. It is, however, important to keep in mind that the splines might add extra information into the system, and thus bias the physics. This problem does not occur with Wannier interpolation, as long as the Fourier coefficients of $\mathcal{T}[\Sigma_{\vec{k}}]$ converge on the real-space cluster.

4. Lattice symmetry

Most of the clusters used in the DCA do generally not obey the same symmetry operations as the infinite lattice. As a consequence, the lattice self-energy in the DCA breaks the symmetry of the lattice due to its strict parametrization with the coarse-grained patches. The only way to resolve this issue in the DCA is to restrict to the few clusters that obey the cluster

symmetry. In order to remove this undesirable feature in the DCA⁺, we symmetrize the self-energy after the interpolation. The interpolated cluster self-energy obeys thus by construction the symmetry operations of the lattice.

B. Cluster deconvolution

The goal of this section is to present a practical implementation of the lattice mapping. As mentioned in the theoretical section of this paper, the lattice mapping is in essence the inversion of the cluster mapping defined in Eq. (20). In a common DCA⁺ calculation, we will have many more basis functions than Monte Carlo cluster points. As a consequence, we need to determine more lattice expansion coefficients than cluster points that are given by the cluster solver. The inversion problem is thus seemingly underdetermined. Therefore, we do not attempt to invert Eq. (20) directly, but first generalize the coarse-graining equation of the self-energy. This is accomplished by rewriting each coarse-graining patch as a translation of the patch around the origin, i.e., $\phi_{\vec{k}}(\vec{k}) = \phi_{\vec{0}}(\vec{k} - \vec{K})$. Next, we generalize the cluster-momentum vector \vec{K} to an arbitrary momentum vector. Using the interpolated cluster self-energy $\bar{\Sigma}_{\vec{k}}$ as a substitute for the cluster self-energy $\Sigma_{\vec{k}}$ in Eq. (19), we obtain

$$\bar{\Sigma}(\vec{k}) = \frac{N_c}{V} \int d\vec{k}' \phi_{\vec{0}}(\vec{k} - \vec{k}') \Sigma(\vec{k}'). \quad (28)$$

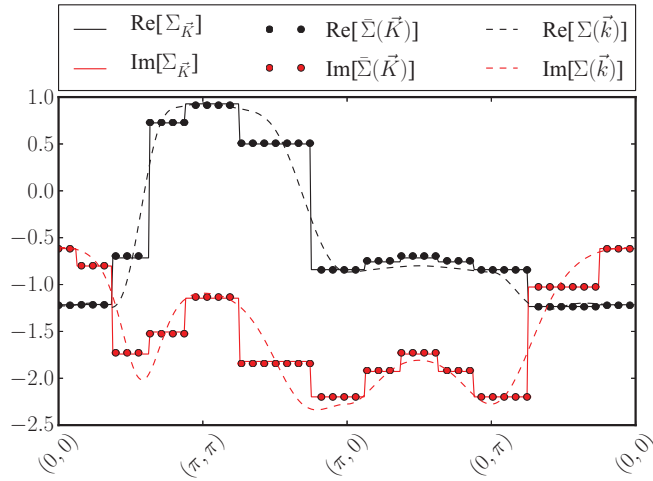


FIG. 6. (Color online) Comparison between the lattice self-energy $\Sigma(\vec{k}, \pi T)$, the cluster self-energy $\Sigma_{\vec{K}}(\pi T)$, and the coarse-grained lattice self-energy at the cluster momenta $\tilde{\Sigma}_{\vec{K}}(\pi T) \equiv \tilde{\Sigma}(\vec{K}, \pi T)$ for a 32-site cluster at 5% doping and $T = 0.2$.

Any solution of Eq. (28) is thus also a solution of Eq. (20). We should stress that with the exception of the continuity of the self-energy, this generalization does not introduce any new information as long as the Wannier interpolation converges! With Eq. (28), we have now rephrased the lattice mapping into a deconvolution problem. These types of problems are regularly encountered in the field of signal theory and image processing and various algorithms have been successfully developed to address the ill-conditioned deconvolution problem.⁴⁴

In this work, we are using a deconvolution algorithm that is based on Bayesian inference, which we discuss in detail in Appendix C. In Fig. 6, we show the lattice self-energy for a 32-site cluster by means of this method. We can clearly observe that the cluster and coarse-grained lattice self-energy coincide very well.

IV. APPLICATION

A. Convergence of the self-energy and the pseudogap

One of the most distinctive features of the hole-doped cuprates is the emergence of a pseudogap,⁴⁵ i.e., a partial suppression of the density of states at the Fermi energy at the antinodal points $(\pi, 0)$ and $(0, \pi)$ in the Brillouin zone. This state appears below a temperature T^* , which rises with decreasing hole doping as the Mott-insulating half-filled state is approached. The detailed relation between the pseudogap and superconductivity remains controversial. Since superconductivity arises from the pseudogap state, it is generally believed that understanding this unusual phenomenon is an important prerequisite to understanding the pairing mechanism. Recent debate has been centered around the question of whether the pseudogap is a signature of superconducting fluctuations above T_c (Refs. 46 and 47) or whether it is a competing phase.^{48,49}

Cluster dynamical mean field studies of the single-band Hubbard model have found a similar pseudogap opening up at the antinodal points at low temperatures in the low-doping regime.^{19,28,50-53} In these calculations, the pseudogap

originates from a strong momentum-space variation of the single-particle self-energy, which, as shown in recent DCA calculations by Gull *et al.*,²⁸ gives rise to a momentum-sector-selective metal-insulator transition. The DCA⁺ improves upon the DCA algorithm in that it gives a self-energy with smooth and therefore more physical momentum dependence, and can therefore provide new insight into this problem. In addition, since previous studies were limited to relatively small clusters up to 16 sites, it is important to explore whether the self-energy and pseudogap physics is converged on such clusters.

In Fig. 7, we plot the imaginary part of the lattice self-energy at the smallest Matsubara frequency $\omega_0 = \pi T$ for various clusters, computed with the DCA (left panel) and the DCA⁺ (right panel). One immediately observes the much more physical smooth momentum dependence of the DCA⁺ results versus the step-function-like nature of the DCA results for the self-energy. At closer inspection, one notices a much more systematic convergence of the DCA⁺ results with different cluster size and geometry. While the DCA results for $\text{Im}\Sigma(\vec{K})$ show smaller spread at a given \vec{K} point [e.g., at $\vec{K} = (\pi, 0)$], their cluster dependence is nonmonotonic. In DCA⁺, in contrast, $|\text{Im}\Sigma(\vec{K})|$ monotonically increases with cluster size, a sensible result as longer-ranged correlations are systematically taken into account.

Another striking feature of the DCA results is the asymmetry for clusters that do not have the full lattice symmetry such as the 16B-, 20-, and 24-site clusters. For example, in the 16B cluster, the asymmetry around $(\pi/2, \pi/2)$ as one moves along the line from $(\pi, 0)$ to $(0, \pi)$ is apparent and the results in these regions are significantly different from those for the symmetric 16A cluster. This asymmetry results from the asymmetric arrangement of the two cluster K points closest to $(\pi/2, \pi/2)$ with respect to $(\pi/2, \pi/2)$ (see right-hand side of Fig. 1). This asymmetry is completely removed in the DCA⁺.

In addition, with the exception of a small region around (π, π) , the DCA⁺ results for the asymmetric 16B cluster are almost identical to the results of the fully symmetric 16A cluster. The DCA⁺ algorithm restores the full lattice symmetry in the results obtained from clusters that do not have the full symmetry and thus makes studies on these clusters much more useful. This, combined with the improved convergence as a function of cluster size allows for much more systematic and precise extrapolations to the exact infinite cluster size.

To further illustrate this point, we now turn to a study of the temperature T^* below which the pseudogap starts to form. Here, we define T^* as the maximum in the temperature dependence of the bulk ($q = 0$) magnetic (particle-hole, spin $S = 1$) susceptibility $\chi_{ph}(q = 0, T)$. The downturn in this quantity below T^* with decreasing temperature signals the suppression of low-energy spin excitations, which is also observed in experiments to accompany the opening of the pseudogap in the single-particle spectral weight. In the DCA and DCA⁺ algorithms, χ_{ph} is computed from the single- and two-particle Green's function G_{ph}^{II} obtained from the cluster solver. Using the notation $K = (\vec{K}, \varpi)$, the bare two-particle Green's function $G_{0,ph}^{II}$ is constructed from a pair of interacting cluster Green's functions (for $\vec{q} = 0$)

$$G_{0,ph}^{II}(K) = G(K)G(K),$$

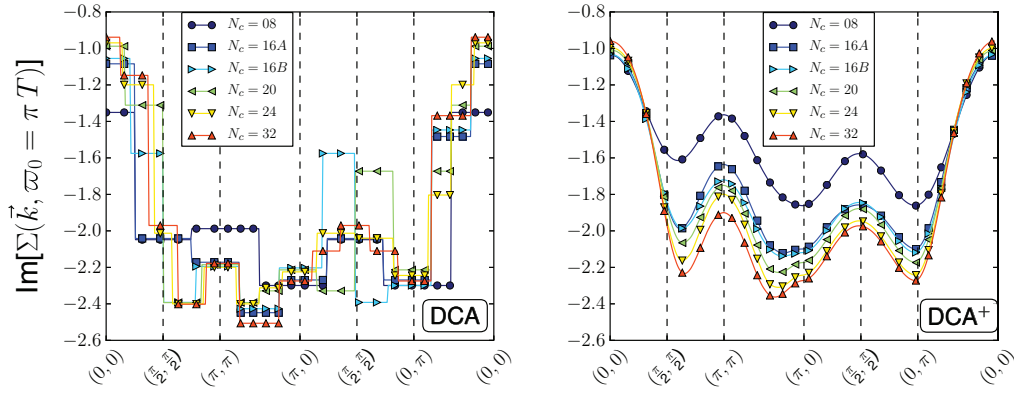


FIG. 7. (Color online) The imaginary part of the lattice self-energy for different clusters at a temperature of $T = 0.33$ with a hole doping of 5% ($U/t = 7$ and $t'/t = -0.15$). Two key observations can be made. The DCA^+ produces for all clusters a lattice self-energy which follows the lattice symmetry. This is not true in the case of the DCA, which is illustrated in the region of $(\pi, 0)$ to $(0, \pi)$ for the clusters 16B, 20, and 24. One can also observe that the DCA^+ converges monotonically. The self-energy increases systematically with increasing cluster size as longer-range correlations are taken into account. This systematic growth of the self-energy is harder to detect in the DCA. Therefore, we expect that the DCA^+ will lead to a more systematic convergence of other physical quantities, such as the pseudogap transition temperature.

while the fully renormalized two-particle Green's function G_{ph}^{II} is computed as

$$G_{ph}^{II}(K, K') = \left(\prod_{l=1}^4 \int_0^\beta d\tau_l \right) e^{i\varpi_1(\tau_1 - \tau_2)} e^{i\varpi_2(\tau_3 - \tau_4)} \times \sum_{\sigma, \sigma' = \pm} \langle c_\sigma^\dagger(\vec{K}, \tau_1) c_\sigma(\vec{K}, \tau_2) c_{\sigma'}^\dagger(\vec{K}', \tau_3) c_{\sigma'}(\vec{K}', \tau_4) \rangle.$$

The irreducible cluster vertex function $\Gamma_{ph}(\vec{Q} = 0, \vec{K}, \vec{K}')$ is then obtained by inverting the Bethe-Salpeter equation on the cluster

$$\Gamma_{ph} = [G_{0,ph}^{II}]^{-1} - [G_{ph}^{II}]^{-1}, \quad (29)$$

where we used a matrix notation in the cluster momenta \vec{K} and \vec{K}' . The uniform lattice spin susceptibility $\chi_{ph}(q = 0)$ is then calculated from

$$\chi_{ph} = \sum_{K_1, K_2} \chi^0 [\mathbb{1} - \Gamma \chi^0]^{-1}.$$

Here, χ^0 is the coarse-grained bare susceptibility of the lattice

$$\chi^0(K) = \int d\vec{k} \phi_K(\vec{k}) G(\vec{k}) G(\vec{k}).$$

This procedure to compute the uniform lattice spin susceptibility $\chi_{ph}(\vec{q} = 0)$ is the same in the DCA^+ as in the DCA.²¹ The quantities that enter these equations, however, are different between both approaches. In the DCA^+ , for thermodynamic consistency, one should apply the same interpolation procedure to the vertex function $\Gamma_{ph}(K, K')$ as is done for the self-energy. Here, however, for the sake of simplicity and in order to focus on the effects of the self-energy, we keep the piecewise constant dependence of $\Gamma_{ph}(K, K')$ that is naturally obtained from its extraction from the cluster quantities in Eq. (29) as in the DCA. In the $S = 1$ particle-hole channel, where the leading correlations are antiferromagnetic and have

only weak internal \vec{K} dependence,⁵⁴ we expect this to be a good approximation.

In Fig. 8, we show results for $\chi_{ph}(\vec{q} = 0)$ obtained with the DCA for different clusters. One observes a strong cluster size dependence and the results are not converged even for the largest cluster that can still be simulated before the fermionic sign problem begins to make the QMC sampling exponentially difficult. The corresponding DCA^+ results are displayed in Fig. 9. Here, convergence is reached much sooner. The location of the maximum in temperature dependence T^* is essentially independent of the cluster for $N_c \geq 20$, as can be seen from Fig. 10. As discussed previously, this directly results from the improved convergence of the self-energy in the DCA^+ . From these results, once the effects of cluster geometry are removed in the DCA^+ , it becomes clear that the underlying correlations that lead to the pseudogap formation are short ranged and well contained in clusters of size 20.

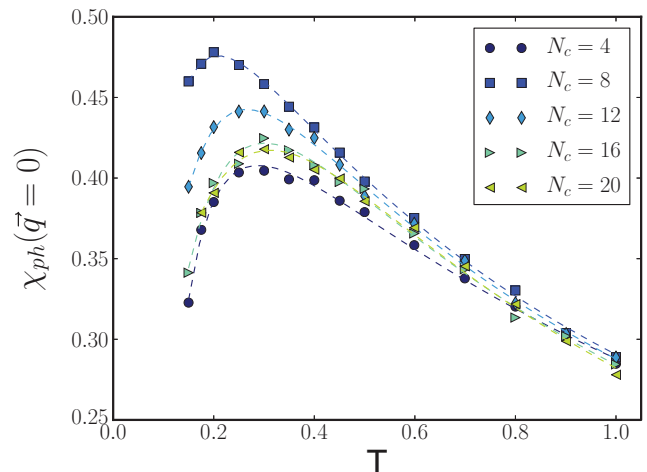


FIG. 8. (Color online) Uniform spin χ_{ph} susceptibilities vs temperature for different cluster computed in the DCA at 5% doping ($U/t = 7$ and $t'/t = -0.15$).

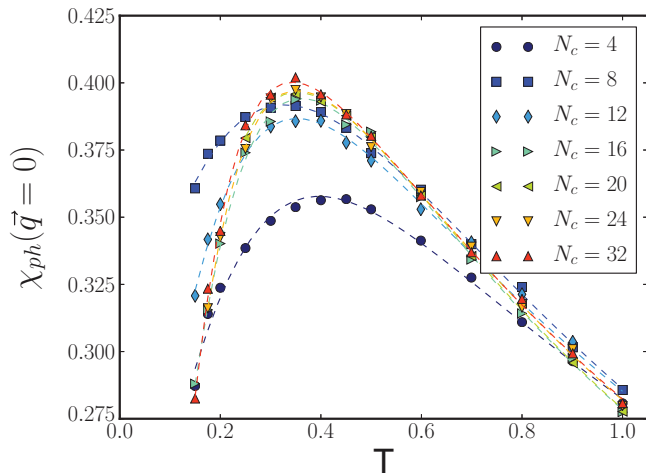


FIG. 9. (Color online) Uniform spin χ_{ph} susceptibilities vs temperature for different cluster computed in the DCA⁺ at 5% doping ($U/t = 7$ and $t'/t = -0.15$).

B. Improved fermionic sign problem

The rapidly increasing capability of computers in conjunction with the growing sophistication and efficiency of quantum Monte Carlo solvers has pushed the limits of simulations to larger cluster sizes and interaction strengths, as well as lower temperatures. As a result, the only serious barrier for quantum Monte Carlo calculations at low temperatures and away from certain parameter regimes (such as half-filling in the single-band Hubbard model) that remains is the fermionic sign problem,²⁴ which leads to an exponentially growing statistical error with increasing system size and interaction strength, and decreasing temperature.

The sign problem has posed an insurmountable challenge to quantum Monte Carlo calculations of fermionic systems, especially for simulations of finite-size systems, and remains a problem in the DCA approach. The DCA, however, was shown to have a less severe sign problem than finite-size calculations,²¹ which, in the absence of a rigorous mathe-

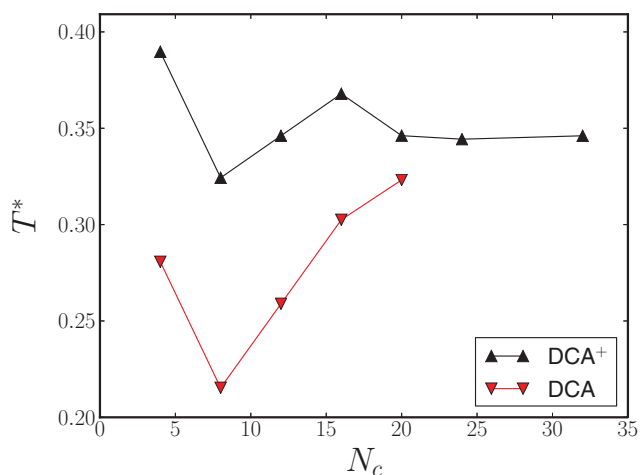


FIG. 10. (Color online) T^* versus cluster size computed in the DCA and DCA⁺ at 5% doping ($U/t = 7$ and $t'/t = -0.15$).

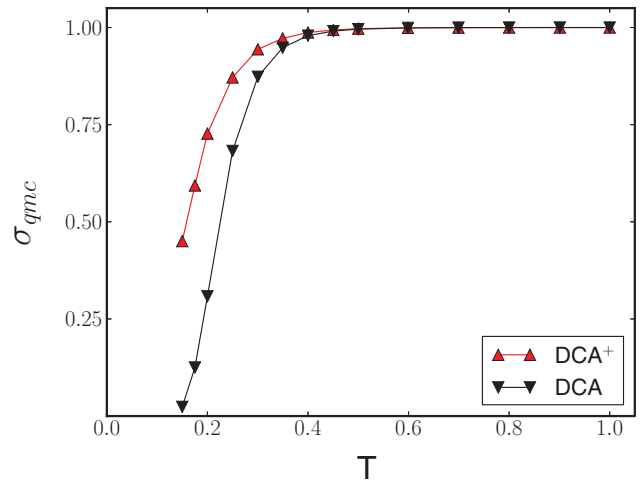


FIG. 11. (Color online) Temperature dependence of the average fermionic sign for $N_c = 32$ at 5% doping ($U/t = 7$ and $t'/t = -0.15$).

matical justification, was attributed to the action of the mean field host on the cluster. This has enabled simulations of larger clusters at lower temperatures than those accessible with finite-size simulations and thus has opened new possibilities for gaining insight into low-temperature phenomena in correlated systems.

The DCA⁺ approach is different from the DCA in that it generates a more physical self-energy with smooth momentum dependence, and the correlations described by this self-energy are therefore shorter ranged than those in the DCA. Hence, it is therefore not unreasonable to expect a difference in the severity of the sign problem between DCA⁺ and DCA.

In Fig. 11, we compare the fermionic sign σ_{qmc} between the DCA and the DCA⁺ for a 32-site cluster and $U = 7t$ for a doping of 5%. At low temperatures, the average sign in the DCA⁺ simulation is significantly larger than that of the DCA simulation. As indicated above, we attribute this improvement to the smooth momentum dependence of the DCA⁺ self-energy as compared to the step-function dependence of the DCA self-energy. From Fourier analysis, one knows that the smoothness of a function is related to the rate of decay of its Fourier coefficients.⁵⁵ More precisely, if a function f is p times differentiable, then its Fourier components f_n will decay at least at a rate of $1/n^{p+1}$:

$$f \in C^p \rightarrow |f_n| \leq \frac{|f^{(p)}|_1}{n^{p+1}}. \quad (30)$$

Since the DCA⁺ self-energy has smooth momentum dependence and not the step discontinuities of the DCA, its Fourier transform to real space is shorter ranged than that of the DCA and the correlations it describes are shorter ranged. We believe that it is this removal of unphysical long-range correlations which reduces the sign problem in the DCA⁺. In any case, with this significant reduction in the severity of the sign problem, it is possible to study the physics of fermionic systems in even larger clusters and at lower temperatures than accessible with the DCA.

V. SUMMARY AND CONCLUSIONS

In this paper, we have presented the theoretical framework as well as a practical implementation of the DCA⁺ algorithm. It is an extension to the DCA without the jump discontinuities inherent in the standard DCA algorithm that computes a continuous lattice self-energy in a self-consistent way. This improvement is based on two fundamental differences to the DCA. First, an explicit distinction is made between the lattice and the cluster self-energy. Second, a continuous lattice self-energy is determined in a way so that its coarse-grained value $\bar{\Sigma}_{\vec{k}}$ is equal to the cluster self-energy $\Sigma_{\vec{k}}$ obtained from the cluster solver. This constraint makes the DCA⁺ algorithm fundamentally different from previous attempts^{20,38} to include a continuous self-energy into the DCA self-consistency loop that lead to an acausal and thus a nonphysical self-energy during the coarse graining of the Green's function but itself has not been coarse grained.

These coarse-graining rules in the cluster mapping of DCA⁺ require us to reconsider the lattice mapping in the algorithm. As a matter of fact, we have shown that a continuous lattice self-energy $\Sigma(\vec{k})$ can only be inferred from the discrete cluster self-energy $\Sigma_{\vec{k}}$ if the DCA assumption of smoothness of the lattice self-energy is satisfied. This has been discussed in the paper using the properties of the projection operator $P_{i,j}$ that is associated with the coarse-graining operation in Eq. (20). The transformation of the cluster self-energy into the lattice self-energy amounts to inversion of the projection operators $P_{i,j}$. Since this is a singular operator, the lattice mapping is only well defined as long as the cluster self-energy converges on the image space of the operator, which is spanned by the eigenvectors with nonzero eigenvalue. In practice, the image space is the space spanned by eigenvectors with an eigenvalue larger than a given parameter ϵ . The convergence behavior of the DCA⁺ algorithm is determined by two essential properties of the projectors $P_{i,j}$: (1) the dimension of the image space increases with cluster size, which is consistent with the intuitive notion that larger cluster can support finer features of the self-energy; (2) the delocalization of each eigenvector $\langle r^2 \rangle$ and the magnitude of its corresponding eigenvalue are anticorrelated. Consequently, for large-cutoff parameter ϵ , a more localized cluster self-energy is needed in order to have a controlled lattice mapping. Self-consistency in the DCA⁺ can only be reached if the cluster self-energy is localized enough to converge on the image space of the projection operator. If convergence is not reached, the image space of the projector and thus the cluster size will have to be increased. Convergence thus provides a useful measure for the quality of a DCA⁺ calculation with a given cluster.

Straightforward inversion of the projection operator would be numerically unstable since the projection operator is a near singular matrix. Thus, in the implementation of the lattice mapping in the DCA⁺ algorithm, we have followed a different approach, splitting it into two numerically stable steps. First, we interpolate the cluster self-energy in a controlled way, using an injective transformation, and next, we deconvolute this interpolated, continuous cluster self-energy using the Richardson-Lucy algorithm. In both steps, convergence within the self-consistent loop can be monitored by an objective measure. For the interpolation, we know that the Fourier

transform of $\mathcal{T}[\Sigma_{\vec{k}}] = (\Sigma_{\vec{k}} - t)^{-1}$ has to converge on the real-space impurity cluster in order to obtain an accurate interpolation. For the deconvolution, the difference between the coarse-grained lattice self-energy $\bar{\Sigma}_{\vec{k}}$ and the cluster self-energy $\Sigma_{\vec{k}}$ has to be smaller than the statistical error of the Monte Carlo integration.

To illustrate the benefits of the DCA⁺ algorithm, we have investigated the pseudogap phase in a lightly hole-doped two-dimensional Hubbard model. Like with the DCA, the DCA⁺ based calculations give a self-energy that has strong momentum dependence. However, we find that the DCA⁺ has a much reduced fermionic sign problem and thus we can investigate the pseudogap phase on larger clusters and in more details than in the standard DCA. In the DCA⁺, the self-energy is continuous in momentum space and thus more physical, and it converges monotonically and much more systematically with cluster size than in the DCA. A similarly improved convergence behavior in the DCA⁺ is found for the pseudogap temperature T^* below which the bulk lattice susceptibility decreases with decreasing temperature. In the DCA, we find that T^* has a strong cluster dependence and converges only for the largest possible cluster sizes. In the case of the DCA⁺, we observe a much faster convergence of T^* , which is a direct consequence of the improved convergence of the self-energy in the DCA⁺. From the convergence property of T^* , we can conclude that the correlations responsible of the pseudogap formation must be short ranged and well contained in a cluster size of eight sites. This improved convergence in the DCA⁺ raises the hope to do precise extrapolations to the exact infinite cluster size limit in future calculations of other properties.

ACKNOWLEDGMENTS

This research was carried out with resources of the Swiss National Supercomputing Center (SCS), Oak Ridge Leadership Computing Facility (OLCF), and the Center for Nanophase Materials Sciences (CNMS). OLCF and CNMS are located at Oak Ridge National Laboratory and supported, respectively, by the Office of Science under Contract No. DE-AC05-00OR22725 and by the Scientific User Facilities Division, Office of Basic Energy Sciences, of the Department of Energy.

APPENDIX A: ANALYSIS OF THE PROJECTION OPERATOR $P_{i,j}$ AND ITS CONNECTION TO THE LOCALITY OF $\Sigma(\vec{k})$.

In this Appendix, we give the reader an intuitive understanding of the projection operator $P_{i,j}$ that plays a central role in the cluster-mapping procedure of the DCA⁺ algorithm. We show that its inverse exists if the DCA locality assumption is satisfied for the lattice self-energy. Furthermore, we discuss how the projection operator $P_{i,j}$ is influenced by the choice of the cluster.

To this end, we expand the lattice self-energy in terms of cubic Hermite splines.⁵⁶ These functions form a basis for cubic splines and obey a convolution property. The lattice self-energy can therefore be written as sum over a very fine mesh $\{\vec{k}_i\}$ in

momentum space

$$\Sigma(\vec{k}) = \sum_{\vec{k}_i} \sigma_{\vec{k}_i} \mathcal{H}(\vec{k} - \vec{k}_i) \quad \text{with} \quad \Sigma(\vec{k}_i) = \sigma_{\vec{k}_i}. \quad (\text{A1})$$

It has to be stressed that choosing Hermite splines as a basis will not influence the conclusions we obtain here and thus does not reduce the generality of our arguments. It just simplifies the discussion since the expansion index i can now be identified with a lattice momentum \vec{k}_i in the fine lattice mesh and the expansion coefficient σ_i with the lattice self-energy at that lattice momentum \vec{k}_i . Next, we generalize the cluster mapping in Eq. (20) by replacing the cluster momentum points $\{\vec{K}_i\}$ by the fine lattice $\{\vec{k}_i\}$. The coarse graining then becomes a convolution of the lattice self-energy with the patches and we obtain

$$\bar{\Sigma}_{\vec{k}_i} = \sum_j \sigma_{\vec{k}_j} \underbrace{\int d\vec{k} \phi_0(\vec{k} - \vec{k}_i) \mathcal{H}(\vec{k} - \vec{k}_j)}_{=P_{\vec{k}_i, \vec{k}_j}}. \quad (\text{A2})$$

The projection matrix $P_{\vec{k}_i, \vec{k}_j}$ has now become a symmetric, square matrix. The latter allows us to do a spectral decomposition of $P_{\vec{k}_i, \vec{k}_j}$ into its eigenspace. If we represent its eigenvalues by λ and its corresponding eigenvector by e_λ , we obtain

$$\bar{\Sigma}_{\vec{k}_i} = \sum_j \sigma_{\vec{k}_j} \sum_\lambda \lambda e_\lambda(\vec{k}_i) \times e_\lambda^T(\vec{k}_j). \quad (\text{A3})$$

In terms of the eigenspace of the projection operator, the cluster and lattice mappings can now be written as

$$\text{cluster mapping:} \quad \bar{\Sigma}_{\vec{k}_i} = \sum_\lambda \lambda \langle \sigma_{\vec{k}_j}, e_\lambda(\vec{k}_j) \rangle e_\lambda(\vec{k}_i), \quad (\text{A4})$$

$$\text{lattice mapping:} \quad \sigma_{\vec{k}_i} = \sum_\lambda \lambda^{-1} \langle \bar{\Sigma}_{\vec{k}_j}, e_\lambda(\vec{k}_j) \rangle e_\lambda(\vec{k}_i).$$

Here, the inner product $\langle \vec{a}, \vec{b} \rangle$ is represented by a simple dot product between the two vectors \vec{a} and \vec{b} . From Eqs. (A4), it is clear that the spectrum $\{\lambda\}$ of the projection operator P_{ij} plays a central role in the cluster and lattice mappings. In Fig. 12, we show the leading eigenvalues (i.e., having the largest absolute value) of $P_{i,j}$ for various clusters. One can clearly observe that all eigenvalues are smaller or equal than one and decay rapidly for small clusters ($N_c \leq 8$) and slowly for large clusters ($N_c \geq 32$). This can be easily understood from the form factor of the patches. The latter are very similar to box-car filters, which are one of the most common low-pass filters used in the field of signal processing. Since the coarse graining of the lattice self-energy in Eq. (A2) can be rewritten as a convolution with the patches, the projection operator $P_{i,j}$ will in fact reduce all the Fourier components during the convolution, ensuring that the L_2 norm of any function in the eigenspace never grows. Consequently, this is also true for all eigenvectors, which leads us to conclude that the eigenvalues have to be less or equal to 1.

With the spectral decomposition of the projection matrix we can split the representation space of the continuous lattice self-energy into the image space \mathcal{I} and the kernel space \mathcal{K} of the projection operator $P_{i,j}$. Since our projection operator does not follow the strict mathematical definition of a projection operator (a projection operator should satisfy the relationship

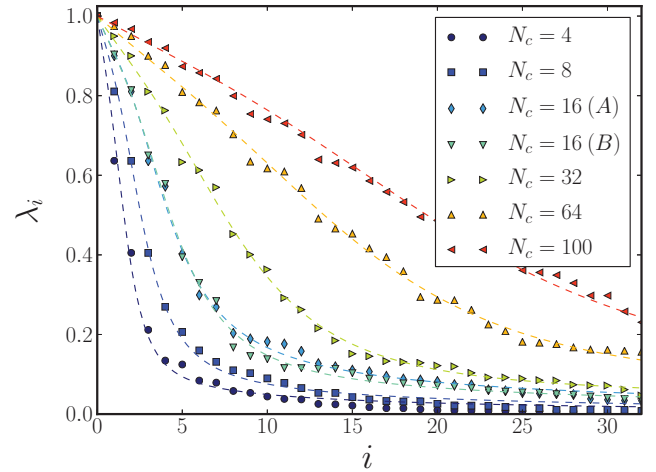


FIG. 12. (Color online) The leading eigenvalues of various clusters on a fine mesh of 512 points. We can clearly observe a strong decay of the leading eigenvalues for small clusters, which becomes weaker with increasing the cluster size. This observation explains the intuitive notion that large clusters can describe finer features in the self-energy since the image space of larger clusters contains more eigenvectors.

$P^2 = P$; the eigenvalues of such an operation can only be 0 and 1), we define the image \mathcal{I}_ϵ as the space spanned by the eigenvectors that have an eigenvalue larger than ϵ . Here, ϵ is a small, positive cutoff parameter. The kernel \mathcal{K}_ϵ contains the remainder of the space and is thus spanned by the eigenvectors with an eigenvalue smaller than ϵ . Due to the inversion of the eigenvalue in Eq. (A4), the lattice mapping is only well defined on the image space \mathcal{I}_ϵ . This brings us to the first important observation. In order to do a self-consistent DCA⁺ calculation, the coarse-grained lattice self-energy should always be entirely defined on the image space \mathcal{I}_ϵ of our projection operator. Otherwise, there exists no well-defined transformation that maps the cluster self-energy back into the lattice self-energy, which in turn breaks the DCA⁺ self-consistency loop. Notice that this requirement holds trivially in the case of the traditional DCA since in that case the projection matrix is simply the identity matrix of size N_c , and all eigenvalues are equal to one.

Equation (A3) can also explain how the geometry of the patches will influence the results obtained with the DCA⁺. In Fig. 13, we plot the union space of the image spaces $\mathcal{I}_{\lambda_i}^A$ and $\mathcal{I}_{\lambda_i}^B$ versus eigenvalue index i for different clusters. The plot shows very clearly that the first leading eigenvectors are equal to each other, and gradually diverge as eigenvectors with smaller eigenvalues are added. This brings us to the second observation. If one wants to carry out a DCA calculation with results that are independent of cluster shape, the cluster self-energy has to be representable on the intersection of the image spaces \mathcal{I}_ϵ of both clusters.

So far, we have only discussed and introduced strict geometrical criteria on the lattice and cluster self-energy, which indicate when a DCA⁺ cluster calculation is feasible. In order to link geometrical criteria to physics, we show in Fig. 14 the delocalization of the leading eigenvectors $\langle r^2 \rangle$. Formally,

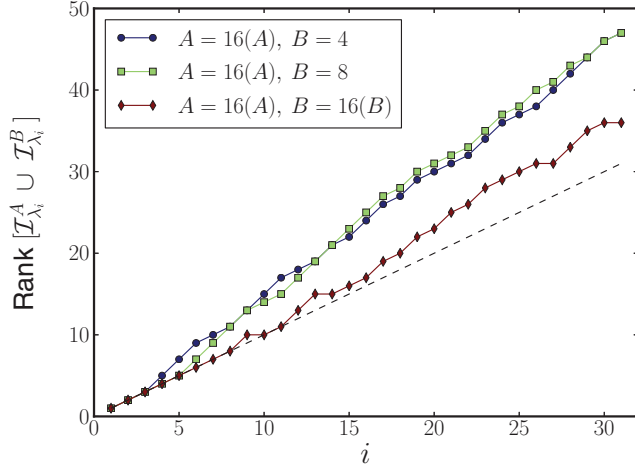


FIG. 13. (Color online) The dimension of the union image space $\mathcal{I}_{\lambda_i}^A \cup \mathcal{I}_{\lambda_i}^B$ for two different clusters A and B versus the eigenvalue index i . Since the rank of $\mathcal{I}_{\lambda_i}^A$ and $\mathcal{I}_{\lambda_i}^B$ both equal i , any deviation of the rank for the space $\mathcal{I}_{\lambda_i}^A \cup \mathcal{I}_{\lambda_i}^B$ from i indicates that the projection operators of clusters A and B span different image spaces. One can clearly observe that the differentiation of the 16A-site cluster eigenspace with smaller clusters occurs faster.

we define the delocalization as

$$\langle r^2 \rangle_\lambda = \sqrt{\frac{\sum_{\vec{r}} e_\lambda^T(\vec{r}) r^2 e_\lambda(\vec{r})}{\sum_{\vec{r}} e_\lambda^T(\vec{r}) e_\lambda(\vec{r})}}. \quad (\text{A5})$$

At close inspection, we can see a clear correlation between the absolute value of the leading eigenvalues λ and the delocalization of its corresponding eigenvector for all cluster sizes. This correlation shows that the space \mathcal{I}_ϵ is actually spanned by the eigenvectors with a small delocalization. As a result, satisfying the geometric criteria to do a self-consistent DCA⁺ calculation is essentially equivalent to satisfying the DCA assumption of locality for the lattice self-energy. Another important conclusion that can be drawn from Fig. 14 is that the number of vectors that span the space $\mathcal{I}_{\epsilon=0.25}$ becomes

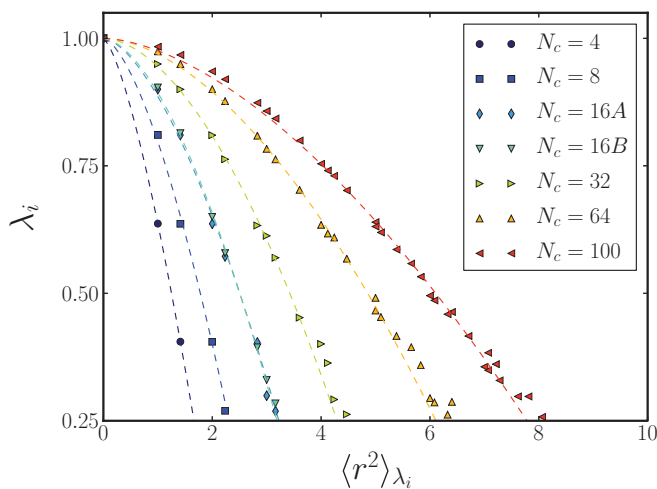


FIG. 14. (Color online) The correlation between the magnitude of the leading eigenvalue and the delocalization of its corresponding eigenvector for various clusters.

larger with increasing cluster size. This correlation reflects the intuitive notion in the DCA that larger clusters can describe finer features of the lattice self-energy.

APPENDIX B: A MATHEMATICAL BASIS FOR THE INTERPOLATION PROCEDURE

In this Appendix, we want to demonstrate that the interpolation procedure presented in this paper is independent of the proposed transformation function \mathcal{T} , as long as the latter is analytical and injective. To accomplish this goal, we construct a function $g(k)$, defined by the transformed real-space Fourier components of an arbitrary function \mathcal{F} that fall within a cutoff parameter R_c . The goal is now to show that $g(k)$ can approximate the function \mathcal{F} with arbitrary precision, given a big enough cutoff parameter R_c . In other words, pointwise convergence of $g(k)$ towards \mathcal{F} is thus guaranteed. The rate of convergence will depend crucially on the rate of convergence of $\mathcal{T}[\mathcal{F}]_R$ versus the radius $|R|$.

Pointwise convergence. Consider a function \mathcal{F} in the Brillouin zone \mathbb{B} and an injective, continuous transformation \mathcal{T} , such that the Fourier components $\mathcal{T}[\mathcal{F}]_R$ fulfill

$$\forall \epsilon > 0, \exists R_c \in \mathbb{R} : \sum_{|R| \geq R_c} |\mathcal{T}[\mathcal{F}]_R| \leq \epsilon$$

with $\mathcal{T}[\mathcal{F}]_R = \int_{\mathbb{B}} d\vec{k} e^{-i\vec{k}R} \mathcal{T}[\mathcal{F}(\vec{k})], \quad (\text{B1})$

then

$$\forall \vec{k} \in \mathbb{B}, \forall \epsilon > 0, \exists R_c \in \mathbb{R} : |g(k) - \mathcal{F}(k)| < \epsilon$$

with $g(k) = \mathcal{T}^{-1} \left[\sum_{R < R_c} \exp(iRk) \mathcal{T}[\mathcal{F}]_R \right]. \quad (\text{B2})$

Choose a positive small number ϵ . Since \mathcal{T} is a continuous and invertible function, we know that the \mathcal{T}^{-1} is also continuous. Hence, by definition of this continuity, there exists a $\delta \in \mathbb{R}_0^+$ for this ϵ , such that

$$|\mathcal{T}[g(k)] - \mathcal{T}[\mathcal{F}(k)]| < \delta \rightarrow |g(k) - \mathcal{F}(k)| < \epsilon.$$

Using the property in Eq. (B1), we can find a radius $R_c > 0$, such that

$$\sum_{|R| \geq R_c} |\mathcal{T}[\mathcal{F}]_R| < \delta. \quad (\text{B3})$$

By the definition of $g(k)$, we have

$$|\mathcal{T}[g(k)] - \mathcal{T}[\mathcal{F}(k)]| = \left| \sum_{R \geq |R_c} \exp(iRk) \mathcal{T}[\mathcal{F}]_R \right| \leq \sum_{R \geq R_c} |\mathcal{T}[\mathcal{F}]_R| \leq \delta. \quad (\text{B4})$$

APPENDIX C: RICHARDSON-LUCY ALGORITHM

One of the most common deconvolution algorithms is the Richardson-Lucy algorithm,^{57,58} which is based on a Bayesian inference scheme. Since the patches are strictly positive and integrate to unity, we can interpret them as a probability

distribution function

$$\forall \vec{k}, \vec{k}': \phi_0(\vec{k} - \vec{k}') \geq 0, \quad 1 = \frac{N_c}{V_{\text{BZ}}} \int_{\text{BZ}} d\vec{k} \phi_0(\vec{k} - \vec{k}').$$

As such, we can apply Bayes theorem and construct a conditional probability \mathcal{Q} for any given lattice self-energy $\Sigma(\vec{K})$:

$$\mathcal{Q}(\vec{k}|\vec{k}') = \frac{\phi_0(\vec{k}' - \vec{k}) \Sigma'_i(\vec{k})}{\int_{\text{BZ}} d\vec{k}'' \phi_0(\vec{k}' - \vec{k}'') \Sigma(\vec{k}'')}. \quad (\text{C1})$$

We should stress at this point that conditional probability \mathcal{Q} is computed separately for the real and imaginary parts of the self-energy. The conditional probability $\mathcal{Q}(\vec{k}|\vec{K})$ is then used to construct a lattice self-energy $\Sigma'(\vec{k})$, given a continuous cluster self-energy $\bar{\Sigma}(\vec{k}')$:

$$\Sigma'(\vec{k}) = \int_{\text{BZ}} d\vec{k}' \mathcal{Q}'(\vec{k}|\vec{k}') \bar{\Sigma}(\vec{k}'). \quad (\text{C2})$$

The idea of the Richardson-Lucy algorithm is now to use Eqs. (C1) and (C2) in an iterative way. After plugging both equations together, we end up with a fixed-point problem

$$\Sigma(\vec{k}) \leftarrow \Sigma(\vec{k}) \int d\vec{k}' \frac{\phi_0(\vec{k} - \vec{k}') \bar{\Sigma}(\vec{k}')}{\int d\vec{k}'' \phi_0(\vec{k}' - \vec{k}'') \Sigma(\vec{k}'')}. \quad (\text{C3})$$

If the interpolated function $\bar{\Sigma}(\vec{k})$ is now used as our initial guess for the lattice self-energy $\Sigma(\vec{k})$, Eq. (C3) provides us with a simple implementation for the lattice mapping. In light of the DCA⁺ algorithm, the Richardson-Lucy deconvolution algorithm has many interesting properties that make it an ideal algorithm to be used for the deconvolution. First of all, it is a straightforward algorithm that does not need any extra, nonphysical input. Other deconvolution algorithms, such as total variation,^{59,60} introduce nonphysical penalty factors to ensure smoothness of the result. Second, the Richardson-Lucy algorithm conserves the sign of strictly positive and negative functions. This property can be easily proven in Eq. (C3) since $\phi_0(\vec{k})$ is strictly positive. Hence, if the initial guess for $\Sigma(\vec{k})$ and $\bar{\Sigma}(\vec{k}')$ are both positive (negative) for all momenta \vec{k} , the resulting $\Sigma(\vec{k})$ will also be positive (negative). Therefore, if the interpolated cluster self-energy $\bar{\Sigma}(\vec{k})$ is causal, the lattice self-energy will also be a causal function. Third, it has been proven that the solution of this iterative scheme converges to the maximum of the likelihood

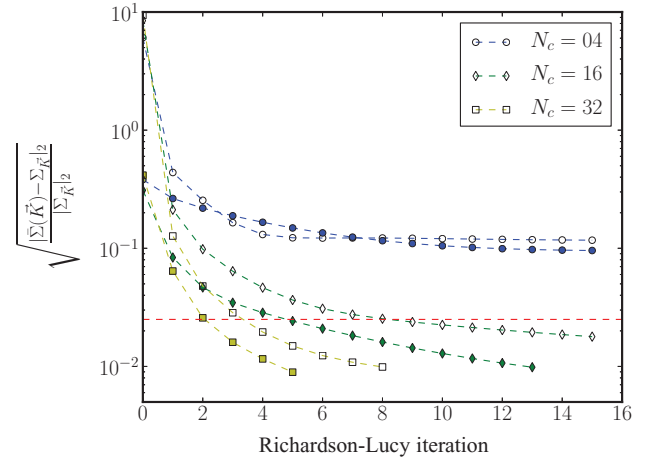


FIG. 15. (Color online) Relative error between the cluster self-energy $\Sigma_{\vec{k}}$ and the integrated lattice self-energy $\bar{\Sigma}(\vec{K})$ for the real (open symbols) and imaginary (solid symbols) parts at 5% doping and $T = 0.2$.

function.⁵⁸ Hence, of all lattice self-energies that generate the same cluster self-energy after the convolution (coarse graining), the Richardson-Lucy algorithm will produce the lattice self-energy that is the most likely to reproduce the cluster self-energy.

Like all other deconvolution algorithms, the Richardson-Lucy algorithm is an approximate algorithm, meaning that the convergence to the exact solution is not guaranteed up to an arbitrary precision. This is not surprising since we know that the convolution is invertible as long as the expansion coefficients of the cluster self-energy in Eq. (A4) decay faster than the eigenvalues of the projection operator. Consequently, the smaller the cluster, the slower the Richardson-Lucy algorithm will converge to a solution and the bigger the discrepancy between the coarse-grained lattice self-energy $\bar{\Sigma}(\vec{K})$ and the cluster self-energy $\Sigma_{\vec{k}}$ obtained from the cluster solver. This phenomenon is illustrated in Fig. 15, where we show the relative error in the L_2 norm between $\bar{\Sigma}(\vec{K})$ and $\Sigma_{\vec{k}}$. The figure clearly shows that the larger cluster converges faster and that the residual error between the cluster and coarse-grained self-energy decreases with increasing cluster size.

¹J. G. Bednorz and K. A. Müller, *Z. Phys. B: Condens. Matter* **64**, 189 (1986).

²T. C. Ozawa and S. M. Kauzlarich, *Sci. Technol. Adv. Mater.* **9**, 033003 (2008).

³A. Georges, W. Krauth, and M. J. Rozenberg, *Rev. Mod. Phys.* **68**, 13 (1996).

⁴V. Anisimov, A. Poteryaev, and M. Korotin, *J. Phys.: Condens. Matter* **9**, 7359 (1997).

⁵V. I. Anisimov, F. Aryasetiawan, and A. I. Lichtenstein, *J. Phys.: Condens. Matter* **9**, 767 (1999).

⁶G. Kotliar and D. Vollhardt, *Phys. Today* **57**(3), 53 (2004).

⁷G. Kotliar, S. Y. Savrasov, and K. Haule, *Rev. Mod. Phys.* **78**, 865 (2006).

⁸A. I. Lichtenstein and M. I. Katsnelson, *Phys. Rev. B* **57**, 6884 (1998).

⁹J. Kuneš, A. V. Lukoyanov, V. I. Anisimov, R. T. Scalettar, and W. E. Pickett, *Nat. Mater.* **7**, 198 (2008).

¹⁰X. Dai, S. Y. Savrasov, G. Kotliar, A. Migliori, H. Ledbetter, and E. Abrahams, *Science* **300**, 953 (2003).

¹¹K. Held, A. K. McMahan, and R. T. Scalettar, *Phys. Rev. Lett.* **87**, 276404 (2001).

¹²K. Held, G. Keller, V. Eyert, D. Vollhardt, and V. I. Anisimov, *Phys. Rev. Lett.* **86**, 5345 (2001).

- ¹³R. J. McQueeney, A. C. Lawson, A. Migliori, T. M. Kelley, B. Fultz, M. Ramos, B. Martinez, J. C. Lashley, and S. C. Vogel, *Phys. Rev. Lett.* **92**, 146401 (2004).
- ¹⁴S. Y. Savrasov, G. Kotliar, and E. Abrahams, *Nature (London)* **410**, 793 (2001).
- ¹⁵J. H. Shim, K. Haule, and G. Kotliar, *Nature (London)* **446**, 513 (2007).
- ¹⁶M. H. Hettler, A. N. Tahvildar-Zadeh, M. Jarrell, T. Pruschke, and H. R. Krishnamurthy, *Phys. Rev. B* **58**, R7475 (1998).
- ¹⁷G. Kotliar, S. Y. Savrasov, G. Pálsson, and G. Biroli, *Phys. Rev. Lett.* **87**, 186401 (2001).
- ¹⁸A. I. Lichtenstein and M. I. Katsnelson, *Phys. Rev. B* **62**, R9283 (2000).
- ¹⁹T. Maier, M. Jarrell, T. Pruschke, and M. Hettler, *Rev. Mod. Phys.* **77**, 1027 (2005).
- ²⁰M. H. Hettler, M. Mukherjee, M. Jarrell, and H. R. Krishnamurthy, *Phys. Rev. B* **61**, 12739 (2000).
- ²¹M. Jarrell, T. Maier, C. Huscroft, and S. Moukouri, *Phys. Rev. B* **64**, 195130 (2001).
- ²²W. Metzner and D. Vollhardt, *Phys. Rev. Lett.* **62**, 324 (1989).
- ²³E. Y. Loh, J. E. Gubernatis, R. T. Scalettar, S. R. White, D. J. Scalapino, and R. L. Sugar, *Phys. Rev. B* **41**, 9301 (1990).
- ²⁴M. Troyer and U. J. Wiese, *Phys. Rev. Lett.* **94**, 170201 (2005).
- ²⁵T. A. Maier, M. Jarrell, T. C. Schulthess, P. R. C. Kent, and J. B. White, *Phys. Rev. Lett.* **95**, 237001 (2005).
- ²⁶P. Staar, T. A. Maier, and T. C. Schulthess, *J. Phys.: Conf. Ser.* **402**, 012015 (2012).
- ²⁷P. Werner, E. Gull, O. Parcollet, and A. J. Millis, *Phys. Rev. B* **80**, 045120 (2009).
- ²⁸E. Gull, M. Ferrero, O. Parcollet, A. Georges, and A. J. Millis, *Phys. Rev. B* **82**, 155101 (2010).
- ²⁹A. Fuhrmann, S. Okamoto, H. Monien, and A. J. Millis, *Phys. Rev. B* **75**, 205118 (2007).
- ³⁰E. Gull, P. Werner, O. Parcollet, and M. Troyer, *Europhys. Lett.* **82**, 57003 (2008).
- ³¹E. Gull, P. Staar, S. Fuchs, P. Nukala, M. S. Summers, T. Pruschke, T. C. Schulthess, and T. Maier, *Phys. Rev. B* **83**, 075122 (2011).
- ³²J. M. Luttinger and J. C. Ward, *Phys. Rev.* **118**, 1417 (1960).
- ³³G. Baym and L. P. Kadanoff, *Phys. Rev.* **124**, 287 (1961).
- ³⁴G. Baym, *Phys. Rev.* **127**, 1391 (1962).
- ³⁵M. Potthoff, *Eur. Phys. J. B* **32**, 429 (2003).
- ³⁶M. Potthoff, *Eur. Phys. J. B* **36**, 335 (2003).
- ³⁷N. Marzari, A. A. Mostofi, J. R. Yates, I. Souza, and D. Vanderbilt, *Rev. Mod. Phys.* **84**, 1419 (2012).
- ³⁸S. Okamoto, A. J. Millis, H. Monien, and A. Fuhrmann, *Phys. Rev. B* **68**, 195121 (2003).
- ³⁹C. De Boor, *A Practical Guide to Splines*, Applied Mathematical Sciences No. 27 (Springer, Berlin, 1978).
- ⁴⁰M. D. Buhmann, in *Radial Basis Functions: Theory and Implementations*, Cambridge Monographs on Applied and Computational Mathematics, Vol. 12 (Cambridge University Press, Cambridge, 2003), p. 259.
- ⁴¹A. A. Abrikosov, L. P. Gorkov, and I. Y. Dzyaloshinskii, *Quantum Field Theoretical Methods in Statistical Physics, International Series of Monographs in Natural Philosophy* (Pergamon, Oxford, 1965).
- ⁴²T. D. Stanescu and G. Kotliar, *Phys. Rev. B* **74**, 125110 (2006).
- ⁴³A. K. Cline, *Commun. ACM* **17**, 218 (1974).
- ⁴⁴P. Jansson, *Deconvolution of Images and Spectra: Second Edition*, Dover Books on Engineering Series (Dover, New York, 2011).
- ⁴⁵M. R. Norman, D. Pines, and C. Kallin, *Adv. Phys.* **54**, 715 (2005).
- ⁴⁶V. J. Emery and S. A. Kivelson, *Nature (London)* **374**, 434 (1995).
- ⁴⁷Y. Wang, N. P. Ong, Z. A. Xu, T. Kakeshita, S. Uchida, D. A. Bonn, R. Liang, and W. N. Hardy, *Phys. Rev. Lett.* **88**, 257003 (2002).
- ⁴⁸L. Taillefer, *Annu. Rev. Condens. Matter Phys.* **1**, 51 (2010).
- ⁴⁹E. Gull, O. Parcollet, and A. J. Millis, *Phys. Rev. Lett.* **110**, 216405 (2013).
- ⁵⁰A. Macridin, M. Jarrell, T. Maier, P. R. C. Kent, and E. D’Azevedo, *Phys. Rev. Lett.* **97**, 036401 (2006).
- ⁵¹O. Parcollet, G. Biroli, and G. Kotliar, *Phys. Rev. Lett.* **92**, 226402 (2004).
- ⁵²B. Kyung, S. S. Kancharla, D. Senechal, A. M. S. Tremblay, M. Civelli, and G. Kotliar, *Phys. Rev. B* **73**, 165114 (2006).
- ⁵³C. Berthod, T. Giamarchi, S. Biermann, and A. Georges, *Phys. Rev. Lett.* **97**, 136401 (2006).
- ⁵⁴N. Bulut, D. J. Scalapino, and S. R. White, *Phys. Rev. B* **47**, 14599 (1993).
- ⁵⁵Y. Katznelson, *An Introduction to Harmonic Analysis*, Cambridge Mathematical Library (Cambridge University Press, Cambridge, UK, 2004).
- ⁵⁶R. Keys, *Acoustics, IEEE Trans. Acoust., Speech, Signal Process.* **29**, 1153 (1981).
- ⁵⁷W. Richardson, *J. Opt. Soc. Am.* **62**, 55 (1972).
- ⁵⁸L. Lucy, *Astron. J.* **79**, 745 (1974).
- ⁵⁹L. I. Rudin, S. Osher, and E. Fatemi, *Physica D (Amsterdam)* **60**, 259 (1992).
- ⁶⁰J. M. Bioucas-Dias, M. A. T. Figueiredo, and J. P. Oliveira, 2006 IEEE International Conference on Acoustics, Speech, and Signal Processing, Vol. 2 (unpublished).